THE JOURNAL OF PHYSICAL CHEMISTRY C

Article

Cite This: J. Phys. Chem. C 2017, 121, 27624−27642

pubs.acs.org/JPCC

First-Principles Study on Polymorphs of $AgVO_3$: Assessing to Structural Stabilities and Pressure-Induced Transitions

Armando Beltrán,[†] Lourdes Gracia,[*,‡] Juan Andrés,[†] and Elson Longo[§]

[†]Departament de Química Física i Analítica, Universitat Jaume I, Campus del Riu Sec, E-12071 Castelló de la Plana, Spain

[‡]Department of Physical Chemistry, University of Valencia (UV), Burjassot 46100, Spain

[§]CDMF-UFSCar, Universidade Federal de São Carlos, P.O. Box 676, 13565-905 São Carlos, SP, Brazil

Supporting Information

ABSTRACT: In this paper, we present a comprehensive theoretical study, based on density-functional theory calculations, and which focuses on the structural and electronic properties of silver vanadium oxide ($AgVO_3$) in the monoclinic [*Cm* (β-$AgVO_3$), *C*2/*c* (α-$AgVO_3$), and *Cc*], orthorhombic (*Amm*2), and cubic ($Pm\bar{3}m$) phases from 0−30 GPa. The structural and electronic properties, the stability of different phases, and the pressure-induced solid−solid phase transitions of $AgVO_3$ have been previously studied. The effects of pressure on the band structures, energy−gap values, density of states, and vibrational frequencies are also studied. Numerical and analytical calculations are conducted to obtain the lattice parameters, the bulk modulus *K* and their pressure derivative *K*′, and the energy-volume equations of state. The influence of different parametrizations of the exchange-correlation functional (B3LYP, HSE06, and PBE) on the investigated properties is analyzed, and the results are compared to available experimental data. For the first time, a complex and unexpected structural and chemical behavior as a function of pressure is reported. The β-phase is the most stable and the first phase transition between the monoclinic β-$AgVO_3$ and *Cc* phase takes place at 5 GPa (B3LYP), 3 GPa (HSE06), and 2 GPa (PBE). There are pressure-induced transitions among the β-, α-monoclinic, and cubic structures, and the corresponding values for the pressure transitions are dependent on the functional used. Two new polymorphs, monoclinic *Cc* and orthorhombic (*Amm*2), have been characterized for the first time, and their contrasting structural stabilities as well as their transition mechanisms can be understood from the intrinsic characteristics of the crystal lattices. The Badger's rule is fulfilled for *Cm*, *Amm*2, and $Pm\bar{3}m$ polymorphs, while it is invalid for the *C*2/*c* and *Cc* phases. Theoretical results show that the studied reactive channels from β-$AgVO_3$ toward binary oxides, Ag_2O and V_2O_5, AgO and VO_2; the elements Ag, V and O_2; silver pyrovanadate, $Ag_4V_2O_7$ and V_2O_5, as well as $Ag_2V_4O_{11}$ and Ag_2O are not thermodynamic favorable processes at pressures up to 30 GPa. These results contribute to the understanding of the pressure behavior of $AgVO_3$-based compounds. In addition, it would be interesting to determine whether further measurements and calculations would confirm the predicted structural and thermodynamic properties as well as the solid-state transformations of $AgVO_3$ polymorphs, which have not yet been experimentally shown.

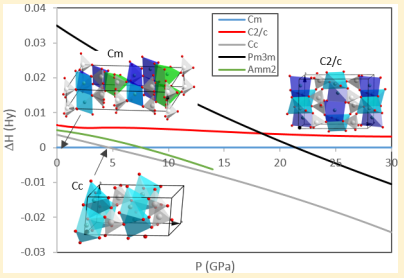

1. INTRODUCTION

External perturbations provoked by pressure are used to modify the electric and optical properties as well as reactivity of solid materials.[1−3] The results derived from high-pressure studies are useful in determining unexpected solid-state transformations as well as the rational design synthesis of inaccessible phases with novel properties which cannot be obtained under ambient pressure.[4−10] Thus, in situ pressure-processing is considered as a fast and clean mechanical method to fabricate new forms of materials with novel properties without the need for chemical reactions or postpurification processes. These innovative materials can appear under high pressure and exhibit physical and chemical properties that are different from their thermodynamically stable counterparts.[11−21] Therefore, analyzing the changes in response to the external pressure yields valuable information that explains the pressure behavior of these materials, providing insight into the factors governing the variation in the structural and electronic changes.[12,19,22,23]

Over the past decade, high-pressure structural studies have gained tremendous momentum, owing to the development of X-ray transparent diamond anvil cells, which provide the foundation for understanding observed high-pressure properties. This has opened the door to studies into polymorphism (i.e., the ability of a material to adopt more than one crystalline structure).[24] The prediction of the propensity of a material toward polymorphism and details of the structure and stability of these phases have attracted significant attention from basic and applied research fields in physics, chemistry, and materials.[24] In recent years, not only the structural stability but also the peculiar physicochemical properties of $AgVO_3$ have attracted considerable interest for practical applications such as batteries, sensors, antibacterial agent, and photocatalysts.[25−42] Their excellent properties can be attributed to the flexibility of their geometric structure, in which both Ag and V cations can adopt different

Received: October 10, 2017
Published: November 17, 2017

DOI: 10.1021/acs.jpcc.7b09865
J. Phys. Chem. C 2017, 121, 27624−27642

local coordination, as well as the electronic properties associated with the hybridization of the valence bands of the V 3d, O 2p, and Ag 4d orbitals, which yield a narrow band gap and highly dispersed valence band.[28]

The understanding of the polymorphism in $AgVO_3$ provides an exciting platform to explore this issue owing to its versatile properties, such as the result of the diverse phase transitions. However, it is very difficult to analyze and characterize the complete polymorph space, presenting a substantial challenge. $AgVO_3$ is known to be polymorphic and exhibits up to four different crystallographic forms, namely α, β, γ, and δ. However, over the past several decades, the structures of both γ and δ-$AgVO_3$ phases have not been well-resolved. Fleury and Kohlmuller presented X-ray diffraction results without structural analysis[43] and further attempts were made to explore the structural chemistry of these phases.[44−48]

β-$AgVO_3$ is a stable phase with a monoclinic space group of *Cm*,[46] while α-$AgVO_3$ is a metastable phase with a monoclinic space group of *C2/c*,[47] which is formed instantaneously just below the melting point when cooled slowly and frozen quickly. An α-$AgVO_3$ polymorph will be irreversibly transformed to β-$AgVO_3$ at 200 °C,[30,44,46,47] while the metastable so-called δ-$AgVO_3$ can be formed by reacting vanadium pentoxide hydrate $V_2O_5{\cdot}nH_2O$ with $AgNO_3$ and their synthesis requires high temperatures.[48,49] Meanwhile, Al-Zaghayer et al.[50] have theoretically characterized the crystalline structure, electronic, optical, and thermoelectric properties of $AgVO_3$ with cubic perovskite, which belongs to the $Pm\bar{3}m$ space group.

From a basic scientific viewpoint, interest has been mainly fueled by both novel synthesis routes to stable, β-$AgVO_3$, and metastable, α-$AgVO_3$, phases, which were developed by our research group.[51,52] Meanwhile, the so-called $\gamma(\delta)$-$AgVO_3$ polymorph can only be synthesized using dedicated high-pressure and high-temperature treatment, and it usually undergoes partial phase transitions upon decompression. In order to pave the way for future investigations along these lines, we perform a complete study to solve the three-dimensional (3D) structure and electronic properties of polymorphs of $AgVO_3$. This study is challenging, especially for metastable systems (i.e., materials that do not occupy the state at the global minimum of the free energy).

First-principles calculations offer the most powerful theoretical tool for studies of the electronic, structural, and optical properties of solid−state materials, and based on our interest in the high-pressure chemistry of complex silver metal oxides such as Ag_2MoO_4,[53] we decided to broaden our research activities into the field of silver vanadium oxides. To the best of our knowledge, a fundamental understanding of the behavior of the different $AgVO_3$ phases at high pressures has not been investigated, either theoretically or experimentally, and information about its physical origin remains unclear. Therefore, their physicochemical characterization is very limited, owing to the inherent phase transition toward to the thermodynamically stable phase. This encouraged us to investigate their geometry, cluster coordination, and electronic structure. The importance of these local coordination environments of Ag and V cations in the lattice and their response to pressure cannot be overstated in providing an understanding into their structure−property relations; these exciting findings have inspired our present theoretical study. However, it is important to recognize that experimentally driven structural refinement approaches typically rely on minimizing the error between simulations from atomic models and the experiment data. This procedure is difficult in complex metal oxides such as $AgVO_3$ systems and, in particular, their metastable phases owing to a large number of available atomic positions and unit cell crystals. In contrast, first-principle calculations can be used to find the correct minimal energy of the metastable configuration for all possible structures with very similar energy.

In this study, we aim to fulfill two objectives. First, we employ first-principle calculations that are based on density functional theory (DFT). It is well-known that the results of DFT depend on the exchange−correlation functional.[54] The influence of different parametrizations of the exchange-correlation functional on the investigated properties will be discussed in detail, and the results are compared to available experimental data. We expect to obtain significant advances in our understanding of the properties and applications of these compounds on the qualitative or semiquantitative level. To do this, we combine experimental data and first-principles calculations. An assessment of the performance of different functional is highly desirable. To guarantee the reliability of our calculations and determine the dependence of our results on the choice of functional, we employ the B3LYP,[55,56] HSE06,[57,58] and PBE[59] functionals. Possible phase transformations have been explored by analyzing the respective equations-of-state (EOS) parameters and by obtaining the corresponding bulk modulus and transition phase pressures. Electronic structures, including DOS and band structures, were calculated based on optimized geometries. The behaviors of these compounds under pressure can be rationalized in terms of the local polyhedral present in the structure. In addition, we analyzed energetic aspects of different dissociation channels used to obtain binary and complex metal oxides, metal, and oxygen. We believe that these novel results may attract sufficient interest because they contribute to broadening the fundamental knowledge of $AgVO_3$-based compounds, in particular, information related to the structural, electronic, and vibrational studies of their polymorphs. Second, a microscopic interpretation of the variation of the relative stability with pressure allows us to construct the high-pressure trend and propose the geometry and electronic structures of new high- pressure polymorphs of $AgVO_3$.

This paper is organized as follows. In section 2, we give an overview of the theoretical procedures and computational methods. In section 3, the results are presented and discussed for the optimized atomic geometries of the five considered phases of $AgVO_3$. In addition, we compare the performances of different exchange-correlation functionals. Finally, we summarize our conclusions in section 4.

2. THEORETICAL METHODS

First-principles total-energy calculations have been carried out within the periodic DFT framework using the CRYSTAL14 software package.[60] The applied density functional approximations were the popular B3LYP[55,56] and HSE06[57,58] hybrid functionals as well as the widely used PBE functional.[59] Moreover, standard functionals do not provide a satisfactory description of van der Waals interactions, which may be important in some compressed systems.[61] For this reason, for the three functionals, the empirical correction scheme to energy that considers the long-range dispersion contributions proposed by Grimme[62] and implemented by Bucko et al.[63] for periodic systems was used. The basic strategy in the development is to restrict the density functional description to shorter electron correlation lengths scales and to describe situations with medium to large interatomic distances using damped $C_6^{ij}{\cdot}R_{ij}^{-6}$ terms, where

DOI: 10.1021/acs.jpcc.7b09865
J. Phys. Chem. C 2017, 121, 27624−27642

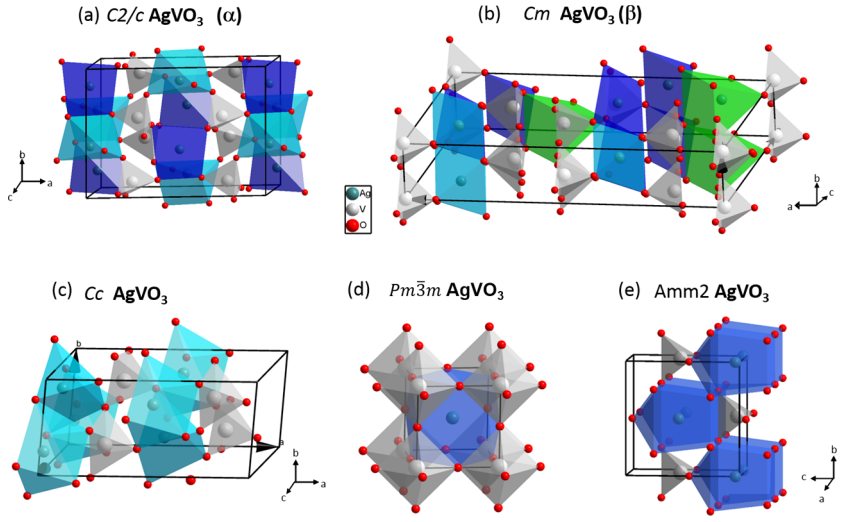

Figure 1. Bulk structure of (a) α -$AgVO_3$, (b) β -$AgVO_3$, (c) monoclinic *Cc*-$AgVO_3$ (d) cubic $Pm\bar{3}m$, and (e) orthorhombic *Amm2*.

C_6^{ij} denotes the dispersion coefficient for atom pair *ij*, and R_{ij} is the corresponding interatomic distance.

Ag, V and O centers have been described by 97-6631d41G, 86-411d31G, and 6-31d1G all electron basis sets, respectively, and are available at the CRYSTAL basis-set site.[64] The diagonalization of the Fock matrix was performed at adequate *k*-point grids in the reciprocal space, which depend on the phase under treatment using Pack−Monkhorst/Gilat shrinking factors (IS = ISP = 4).

The total number of *k*-points was 24 (*C2/c*), 24 (*Cm*), 24 (*C2/c*), 21 (*Amm2*), 10 ($Pm\bar{3}m$) for the $AgVO_3$ polymorphs, 27 for V_2O_5 (*Pmmn*) and 10 for Ag_2O ($Pn3m$), 18 for VO_2 ($P4_2/mnm$) and 14 for AgO ($I4_1/a$), 27 for $Ag_4V_2O_7$ (*Pbca*), and 24 for $Ag_2V_4O_{11}$ ($C2/m$) phases, respectively. The vibrational frequencies were obtained at the Γ point within the harmonic approximation; the dynamic matrix was computed by the numerical evaluation of the first derivative of analytical atomic gradients. To consider the effect of pressure on the vibrational frequencies and the electronic structure of this system, we optimized geometric parameters and internal positions of all phases, at a number of fixed external pressures that range from 0−30 GPa. The technical details of corresponding optimization procedures are given in the Supporting Information.

The CRYSTAL program can perform an automated scan over the volume to compute energy−volume ($E-V$) curves.[65] Optimized $E-V$ data are fitted to the 3th order static Birch−Murnaghan (BM) EOS.[66,67] From: $P = -\frac{\partial E}{\partial V}$, the pressure−volume ($P-V$) connection is established. As a result, the pressure-dependence of the atomic and electronic structure was determined, such as the zero-pressure bulk modulus, K_0, given by $K_0 = -V\frac{\partial P}{\partial V} = V\frac{\partial^2 E}{\partial^2 V}$, and its pressure derivative, K_0', values as well as $V-P$ dependence of the total energy and enthalpy. Following this procedure, enthalpy−pressure curves have been obtained for the five $AgVO_3$ polymorphs as well as for the constituent oxides Ag_2O and V_2O_5 and the corresponding values of pressure for induced phase transitions have been calculated. The electronic structures, including the density of state (DOS) and band structures, were calculated based on the optimized geometries.

We also calculated the dependence of the enthalpy on pressure for the polymorphs of $AgVO_3$ with different types of functional: B3LYP, HSE06, and PBE. Four types of reactive channels have been studied and the corresponding enthalpy, $\Delta_r H$, is calculated using the following equations:

(i) Formation of metal oxides

$$\Delta_r H = \sum_{i}^{\text{metaloxides}} H_i - H_{AgVO_3}$$

(ii) Formation of metals and oxygen

$$\Delta_r H = H_{Ag} + H_V + \frac{3}{2}H_{O_2} - H_{AgVO_3}$$

(iii) Formation of $Ag_4V_2O_7$ and V_2O_5

$$\Delta_r H = \frac{1}{4}H_{Ag_4V_2O_7} + \frac{1}{4}H_{V_2O_5} - H_{AgVO_3}$$

(iv) Formation of $Ag_2V_4O_{11}$ and Ag_2O

$$\Delta_r H = \frac{1}{4}H_{Ag_2V_4O_{11}} + \frac{1}{4}H_{Ag_2O} - H_{AgVO_3}$$

where $H_i^0 = E_T + pV$. Here, E_T is the total energy, for the most stable solid polymorphs of each structure at $P = 0$ are considered in our calculations, and the corresponding equilibrium structures were obtained by optimizing all of the geometric parameters.

To minimize errors due to the incorrect estimation of the O_2 binding energy, which is significantly overestimated by 1−1.5 eV when the standard DFT functional is used,[68−71] we employed a water reference instead of a molecular oxygen-based reference,[71] following the equation: $\frac{1}{2}H_{O2} = H_{O2} - H^0_{H_2}$.

3. RESULTS

3.1. Crystalline Structure and Equation of State. In order to study the influence of different approximations for exchange and correlation on the DFT results for $AgVO_3$, we perform complete structure optimizations of the lattice parameters and the atomic displacements for five phases using the B3LYP, HSE06, and PBE functionals. A polyhedral representation for the monoclinic (*Cm*, *C2/c*) and cubic ($Pm\bar{3}m$) together with two predicted novel phases: monoclinic

DOI: 10.1021/acs.jpcc.7b09865
J. Phys. Chem. C 2017, 121, 27624−27642

Table 1. Calculated B3LYP and Available Experimental Values of the Cell Parameters as well as Bulk Modulus (K_0) and its Pressure Derivative (K_0') for $AgVO_3$ Geometries[a]

(a)

*C*2/*c*	B3LYP	HSE06	PBE	exptl[47]	exptl[52]
a (Å)	11.4094 (+9.3)	11.5684 (+10.8)	11.6471 (+11.6)	10.4370	10.4355−10.4561
b (Å)	8.1853 (−17.3)	7.2751 (−26.5)	7.3732 (−25.5)	9.8970	9.9221−9.9245
c (Å)	5.8926 (+6.5)	5.9700 (+6.1)	6.0691 (+9.7)	5.5320	5.5171−5.5223
β (deg)	106.38 (+6.7)	108.25 (+8.6)	109.43 (+9.8)	99.69	99.54−99.59
V_0 (Å^3)	527.98 (−6.4)	493.34 (−12.4)	491.66 (−12.7)	563.28	563.36−565.07
K_0 (GPa)	40.68	68.30	91.27		
K_0'	10.45	10.53	4.35		
Cm	B3LYP	HSE06	PBE	exp[46]	exp[51]
a (Å)	17.7588 (−1.9)	17.4793 (−3.5)	17.4244 (−3.8)	18.1060	18.104−18.123
b (Å)	3.5564 (−0.6)	3.5452 (−0.9)	3.5448 (−0.9)	3.5787	3.578−3.579
c (Å)	8.2060 (+2.0)	8.1161 (+0.9)	8.1379 (+1.2)	8.0430	8.043−8.044
β (deg)	103.51 (−0.9)	103.65 (−0.8)	103.48 (−0.9)	104.44	104.47−104.50
V_0 (Å^3)	503.94 (−0.14)	488.90 (−3.1)	493.10 (−2.3)	504.69	
K_0 (GPa)	118.09	126.26	121.68		
K_0'	4.83	4.44	4.63		

Cc	B3LYP	HSE06	PBE
a (Å)	10.6182	10.3800	10.4050
b (Å)	5.0466	5.0214	5.0568
c (Å)	5.0249	5.0003	5.0338
β (deg)	117.91	118.36	118.57
V_0 (Å^3)	237.95	229.34	232.61
K_0 (GPa)	127.86	119.37	115.95
K_0'	0.86	0.37	2.36

(b)

Pm3m	B3LYP	HSE06	PBE	theor[50]
a (Å)	3.7734	3.7674	3.7818	3.752
V_0 (Å^3)	53.75	52.21	54.09	52.82
K_0 (GPa)	232.55	247.79	221.49	219.45
K_0'	3.88	3.85	3.91	4.86

*Amm*2	B3LYP	HSE06	PBE
a (Å)	3.4079	3.4487	3.5446
b (Å)	6.0098	5.7993	5.7284
c (Å)	5.9852	5.8014	5.7299
V_0 (Å^3)	122.58	116.03	116.35
K_0 (GPa)	66.79	63.57	76.57
K_0'	4.21	9.91	13.80

[a]Data in brackets represent relative deviations from the experimental (a) and (c) values in percent, for *C*2/*c* and *Cm* structures, respectively.

Cc and orthorhombic (*Amm*2) are shown at ambient pressure in Figure 1.

In addition, we searched for a minimum in the $AgVO_3$ tetragonal (*P*4*mm*) and hexagonal ($P6_3/mmc$) structures. However, all attempts were unsuccessful; for the $AgVO_3$ tetragonal, the optimized geometry presents one imaginary frequency, around −380 cm^{-1}, which is associated with the E mode of the O−V−O bending mode, while for the $AgVO_3$ hexagonal, several imaginary frequencies have been found. Therefore, these structures are unstable and were not considered (in Table S1 and Figure S1 the corresponding geometries are given).

Optimized lattice parameters and equilibrium volume for the five $AgVO_3$ phases, together with the available experimental data for the *C*2/*c* and *Cm* monoclinic phases, at ambient pressure are presented in Table 1. An analysis and comparison of the results reported in Table 1a shows that calculated parameters for both *C*2/*c* and *Cm*-$AgVO_3$ structures are in reasonable agreement with previous experimental reported data. At the B3LYP level, the relaxed lattice parameters obtained from calculations differed (in percent) from the experimental values by −1.9%, −0.6%, + 2.0%, and −0.9% for *a*, *b*, and *c* lattice parameters and *β* angle of *Cm* $AgVO_3$, respectively; however, the difference in volume is less than −0.15%. However, for the *C*2/*c* $AgVO_3$ structure, the agreement with the experimental data is lower, with the differences +9.3%, −17.3%, + 6.5%, and +6.7% for the *a*, *b*, and *c* lattice parameters, and the *β* angle, respectively, with the volume difference being −6.4%.

The calculated geometric HSE06 values are close to the PBE ones, and also a lower accord with the *C*2/*c*-$AgVO_3$ experimental data is found (−12.4% and −12.7%, for the relaxed volumes). For −*Cm*-$AgVO_3$−, the corresponding discrepancies with the experimental volume are only −3.1% and 2.3%, for those calculated at the HSE06 and PBE levels, respectively.

For the cubic phase, the calculated structural data are in agreement with the PBE calculations reported by Al-Zaghayer et al.[50] The corresponding cell parameters calculated using the three functionals are given in Table 1b.

DOI: 10.1021/acs.jpcc.7b09865
J. Phys. Chem. C 2017, 121, 27624−27642

The local coordination of V cations in both α-AgVO3 ($C2/c$) and β-AgVO3 (Cm) is four, forming [VO_4] tetrahedral clusters. Only one type of V site is present in the $C2/c$-AgVO3, forming an almost regular tetrahedron with O anions, in contrast to the four types of distorted tetrahedral polyhedra in Cm–$AgVO_3$ (see Figure 1). There are two types of Ag sites in $C2/c$–$AgVO_3$, forming distorted octahedra, [AgO_6], which are expanded to the c-direction by sharing the edges. α-$AgVO_3$ presents empty polyhedra that comprise six oxygen atoms that form a distorted triangular O6 prism linked to empty O8 polyhedra in which eight oxygen anions are coordinated. The total empty volume represents 72.7% of the total cell volume at ambient pressure.

The β-$AgVO_3$ structure forms zigzag chains of [VO_4] tetrahedra in which 5-, 6-, and 7-coordinated polyhedra formed by O atoms are occupied by three types of Ag cations: the first Ag cation forms [AgO_6] distorted octahedra (Ag1), with a mean bond distance of 2.417 Å; the second and third Ag cations (Ag2 and Ag3) were positioned in a [AgO_5] square pyramid, where the Ag–O bonds were similar in magnitude and have a mean bond distance of 2.400 Å; the fourth Ag cation was a seven coordinate, [AgO_7] distorted deltahedra, where the Ag–O bond lengths ranged from 2.368 to 3.026 Å.[44,46,72] β-AgVO3 presents an unoccupied volume that consists mainly of channels of rhombohedral section of O8 polyhedra linked to form channels along the b direction as well as channels of O7 polyhedra linked to form channels of triangular section also along the b direction. Here the empty volume represents 58.4% of the unit cell volume at ambient pressure.

The Cc monoclinic $AgVO_3$ contains only one type of Ag cation, coordinated with seven oxygen anions, [AgO_7], while the number of oxygen anions coordinated with the V cations is five (actually 3 + 2), forming a distorted [VO_5] cluster. Cc -AgVO3 presents empty channels along the c direction with a triangular section formed by unoccupied 7-fold coordinated O7 polyhedra, which represents 56.2% of the unit cell volume at ambient pressure. The corresponding cell parameters can be found in Table 1. A lower coordination number of the V cations is associated with strong interactions between the V cations and oxygen anions.

In the cubic ($Pm\bar{3}m$) structure, the V cations are located at the centers of regular oxygen octahedral, [VO_6], forming layers and are linked by the oxygen atoms in [AgO_{12}] regular polyhedra, and they completely fill the unit cell volume.

The orthorhombic ($Amm2$) structure shows silver atoms that are 9-fold-coordinated to oxygen atoms forming [AgO_9] polyhedral chains linked between them by [VO_4] units. They present empty channels along the a direction, having triangular section formed by unoccupied 8-fold-coordinated O8 polyhedra. Here the total volume of the empty polyhedra represents 68.8% of the total cell volume at ambient pressure. Calculated cell parameters for this structure can be found in Table 1b.

The energetic ordering of the different phases at ambient pressure for the three functionals is monoclinic (Cm) < monoclinic (Cc) < orthorhombic ($Amm2$) < monoclinic ($C2/c$) ≪ cubic ($Pm\bar{3}m$), where the relative energy of the cubic structure is very high. It is well-known that the choice of the exchange-correlation functional as well as the fraction of exact exchange in various hybrid functionals alter the phase stability of oxide systems (see Table 2).[73−80]

Figure 2 illustrates the correlation between the equilibrium unit-cell volume V and the total energy difference per formula unit ΔE with respect to the Cm monoclinic phase calculated with different functionals. The dashed bars indicate the total volume and energy ranges, encompassing all five phases for a particular functional. The remarkably widespread at both the relative energy and volume of the B3LYP results for the different phases are clearly visible. Figure 2 shows a close dependence between the relative and unit-cell volume, indicating that there is a dominant volume effect on the phase stability of the $AgVO_3$ polymorphs [i.e., the most stable phases (Cm, Cc, $Amm2$, and $C2/c$) present the largest volume with respect to the less stable ($Pm\bar{3}m$). An analysis of the results shows that each polymorph can be associated with a specific region on this representation for the three functionals. At these regions, the B3LYP results exhibit the largest values for the volume, except for the $Pm\bar{3}m$ phase. The body of data for the structure, geometry, and phase energetics suggests that there is no good justification for sticking with B3LYP, HSE06, or PBE when dealing with complex oxide materials such as $AgVO_3$. All three functionals provide a sound basis for subsequent calculations.

Table 2. Computed Energy Differences [a.u. ($/10^{-3}$) /f.u.] between Different Structural Phases of $AgVO_3$ at P = 0 GPa Relative to the Monoclinic Cm Phase [E-E(Cm)]

	B3LYP	HSE06	PBE
monoclinic (Cc)	3.7	1.7	1.1
orthorhombic ($Amm2$)	5.0	3.5	3.6
monoclinic ($C2/c$)	6.4	6.9	6.8
cubic ($Pm\bar{3}m$)	47.3	29.1	20.2

Future studies appear to be well-suited as a starting point not only for hybrid-functional DFT involving more recent parametrizations, such as PBEsol, AM05, or meta-GGAs, which are constructed to satisfy a maximum number of exact constraints for the exchange-correlation functional without empirical parameters, but also for higher level perturbative approaches within the framework of many-body perturbation theory,[81] which can offer a reliable and numerically efficient way of improving the accuracy of state-of-the-art ab initio simulations.

3.2. Vibrational Properties. Lattice vibrations and their behavior under pressure provides useful information regarding structural instabilities and phase transformations. Group theoretical considerations of the β-$AgVO_3$ structure in the Cm space group indicates 57 Raman-active modes matching the following decomposition at the Γ point: (Γ = 38A′ + 19A″), to which the acoustic modes (2A′ + 1A″) should be added.[82] Table 3 shows the calculated B3LYP frequencies (ω) of the Raman-active modes at the Γ point for the (a) $C2/c$, (b) Cm, (c) Cc, and (d) $Amm2$ structures as well as the Grüneisen parameters, $\gamma = [B_0/\omega_0]\, d\omega/dP$, which have been calculated using the B_0 value reported in Table 1.

For simplicity, the results of the B3LYP calculations are first discussed, and, if necessary, the deviations with respect to the two other functionals are highlighted. de Oliveira et al. identified Cm-$AgVO_3$ 15 Raman-active modes experimentally.[51] The peak at 943 cm^{-1} (experimental 947 cm^{-1}) corresponds to the symmetric stretching of the VO_4 units. The peak that is located at 885 (exptl 884) cm^{-1} is due to stretching vibrations of O–V–O. The band at 862 (exptl 845) cm^{-1} may be associated with the stretching vibrations of VO groups in the $(V_2O_7)^{4-}$ ion. The band at 820 (exptl 804) cm^{-1} may be assigned to stretching vibrations of the Ag–O–Ag bridges. In addition, the bridging V–O–Ag and V–O–V asymmetric stretching in the polymeric metavanadate chains and the bending modes of [VO_4] give rise to bands that are located at 711 (exptl 701) and 755 (exptl 731) cm^{-1}. The bridging V–O–Ag asymmetric stretching bonds in

DOI: 10.1021/acs.jpcc.7b09865
J. Phys. Chem. C 2017, 121, 27624−27642

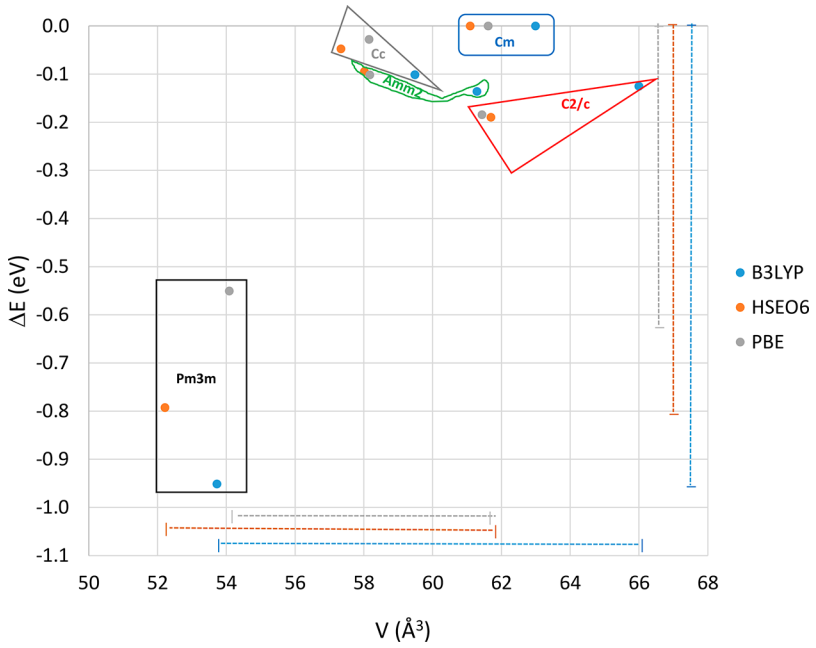

Figure 2. Correlation between the equilibrium unit-cell volume V and the total-energy difference per formula unit ΔE with respect to the *Cm* monoclinic phase calculated with different functionals. The dashed bars indicate the total volume and energy ranges encompassing all seven phases for a particular functional.

the metavanadate chains and to the V−O−V stretches bond is reflected by the band located at 520 (exptl 514 exptl) cm^{-1}. The Raman bands at 393 (exptl 383) and 335 (exptl 334) cm^{-1} may be assigned to the asymmetric deformation modes of the $[VO_4]$ tetrahedron. These peaks along with those located at 272 (exptl 272), 256 (exptl 246), 233 (exptl 226), 124 (exptl 121), and 169 (exptl 161) cm^{-1} indicate the channel-structured β-$AgVO_3$ structure. All of the *Cm*-$AgVO_3$ Raman-active modes are characterized by an increase of the vibrational frequency with pressure (positive Grüneisen parameter), and they do not present discontinuities in the pressure dependence of the total energy (see below). This feature confirms that the transition *Cm*-to-*Cc* monoclinic structures is a first-order transition.

The α-$AgVO_3$ structure in the *C*2/*c* space group presents the following 30 Raman active modes: (Γ = 14Ag + 16Bg). The corresponding calculated frequencies are provided in Table 3a together with recently published experimental data.[83] On the other hand, six *C*2/c-$AgVO_3$ modes have negative values for γ at 675.44 (Ag), 833.45 (Bg), 937.51(Ag), 954.34 (Ag), 1007.70 (Bg), and 1008.81 (Ag) cm^{-1}.

The monoclinic *Cc*-$AgVO_3$ structure presents the following Raman active modes: (Γ = 13A′ + 14A″) to which the acoustic modes (2A′ + 1A″) should be added. The calculated values of the corresponding frequencies can be found in Table 3c from ambient to 10 GPa. For this structure, the evolution of the frequency values with pressure can be divided into three different regions: from ambient to 10 GPa, from 10 to 15 GPa and from 15 to 30 GPa. For instance, the A″ mode of 534.46 cm^{-1} at ambient pressure has a frequency of 532.65 cm^{-1} at 10 GPa, but it is 493.53 cm^{-1} at 15 GPa and 515.95 cm^{-1} at 30 GPa. Three *Cc*-$AgVO_3$ modes have negative values for γ between 0 and 10 GPa but have positive γ values that are between 15 and 30 GPa. On the other hand, there are four modes that present positive γ values between 0 and 10 GPa, while between 15 and 30 GPa there are negative values for γ. As we can see in Table 3c, all the γ values between 15 and 30 GPa are lower than the corresponding values between 0 and 10 GPa. This behavior may be related to the change of the cell parameters versus pressure, which takes place between 10 and 15 GPa (see the next section). The cubic $Pm\bar{3}m$-$AgVO_3$ does not present any Raman active mode and all of the IR active frequencies increase uniformly with pressure.

The orthorhombic *Amm*2-$AgVO_3$ structure presents the following Raman active modes: ($\Gamma = 4A_1 + A_2 + 3B_1 + 4B_2$) to which the acoustic modes ($A_1 + B_1 + B_2$) should be added. With the exception of A_2, all modes are also IR active. Details are provided in Table 3d. Six *Amm*2-$AgVO_3$ modes have negative values for γ, and it is important to note that the B_2 mode of 105 cm^{-1} at ambient pressure presents a particular behavior, in that its frequency increases from ambient to 10 GPa and decreases above 10 GPa being negative at 15 GPa and above. At ambient pressure, this vibrational mode is associated with the bending of the Ag−O−V angle, but at 15 GPa, the B_2 mode of −58 cm^{-1} is characterized by the torsion of the $[VO_4]$ tetrahedron with respect to the $[AgO_9]$ polyhedral chains. The impracticability of further compressing this structure along the [100] direction leads to the torsion of the $[VO_4]$ units, which causes structural. In addition, HSE06 and PBE calculations show negative frequency values for the B_2 mode above 15 and 5 GPa, respectively.

3.3. Pressure Effects. The overall effect of pressure on the volume and unit cell parameters for the five polymorphs is presented in Figure 3.

The volumes of all $AgVO_3$ structures decrease uniformly against pressure with all functionals, and near 30 GPa the volumes of the *Cc* and $Pm\bar{3}m$ polymorphs become practically the same as B3LYP, as well as those of the *Cm* and *C*2/*c* $AgVO_3$ with B3LYP and PBE functionals. The B3LYP $Pm\bar{3}m$ structure always has the lowest volume (per unit formula) up to 28 GPa, and above this pressure, it is the *Cc* phase, while with HSE06 calculations, the *Cc* phase has the lowest volume above 19 GPa.

As we can see in Figure 3a, the unit−cell volume of the *C*2/*c* $AgVO_3$ exhibits a high compressible trend with a volume reduction of about 12.2% from ambient up to 10 GPa, followed

DOI: 10.1021/acs.jpcc.7b09865
J. Phys. Chem. C 2017, 121, 27624−27642

Table 3. Calculated Raman Frequencies and the Corresponding Grüneisen Parameters for the (a) *C2/c*, (b) *Cm*, (c) *Cc*, and (d) *Amm2* Structures

(a) *C2/c*

Raman mode	ω (cm^{-1})	γ^a	exptl[83] (cm^{-1})
B_g	68.08	0.89	
A_g	68.27	1.86	
A_g	74.49	1.63	
B_g	74.62	1.91	
B_g	95.25	0.96	
B_g	111.86	0.41	
B_g	128.85	0.53	
A_g	138.77	0.83	
A_g	153.93	1.42	
A_g	185.02	0.92	
B_g	194.69	0.81	
A_g	217.88	0.50	
B_g	226.09	0.80	
B_g	248.76	0.93	
A_g	257.44	0.80	
B_g	298.14	0.20	
A_g	301.98	0.17	
B_g	334.54	0.46	330
B_g	381.75	0.49	
A_g	403.58	0.25	
B_g	444.73	0.30	
A_g	449.22	0.44	
A_g	554.47	0.12	
B_g	579.43	0.15	
A_g	675.44	−0.04	737
B_g	833.45	−0.19	812
A_g	937.51	−0.36	849
B_g	954.34	−0.01	892
B_g	1007.70	−0.08	924
A_g	1008.81	−0.09	956

(b) *Cm*

Raman mode	ω (cm^{-1})	γ^a	exptl (cm^{-1})	Raman mode	ω (cm^{-1})	γ^a	exptl (cm^{-1})
(A′)	54.95	2.55		(A″)	326.65	0.95	
(A″)	65.12	1.13		(A″)	330.92	1.11	
(A″)	83.41	0.32		(A′)	335.03	1.04	334.29
(A′)	84.59	0.39		(A″)	344.38	1.46	
(A′)	90.46	0.28		(A′)	376.71	0.32	
(A″)	91.21	0.21		(A′)	393.30	0.24	383.12
(A′)	93.65	1.17		(A′)	405.98	0.35	
(A′)	102.90	1.77		(A′)	435.24	0.28	
(A′)	119.23	1.81		(A′)	452.18	0.57	442.08
(A″)	124.45	1.36	121.70	(A′)	465.93	0.29	
(A′)	129.41	1.89		(A′)	488.62	0.18	
(A″)	133.43	1.86		(A″)	520.00	0.45	514.58
(A′)	142.69	2.31		(A′)	525.04	0.63	
(A′)	169.68	2.19	161.90	(A′)	537.23	0.40	
(A′)	173.38	2.54		(A″)	546.69	0.64	
(A′)	184.88	1.90		(A′)	549.12	0.56	
(A′)	191.94	1.45		(A′)	562.74	0.65	
(A″)	194.39	1.52		(A″)	711.40	0.67	701.55
(A″)	196.82	1.78		(A″)	754.88	0.68	731.88−737[b]
(A′)	210.73	1.72		(A′)	820.03	0.27	804.39−815[b]
(A′)	233.05	1.33	226.72	(A′)	862.78	0.22	845.26
(A″)	256.23	0.42	246.86	(A′)	885.38	0.13	884.42−892[b]
(A′)	258.39	1.01		(A′)	909.00	0.21	
(A′)	261.47	1.11		(A′)	943.00	0.29	947.46
(A″)	267.15	1.00					
(A′)	272.77	1.35	272.54				

DOI: 10.1021/acs.jpcc.7b09865
J. Phys. Chem. C 2017, 121, 27624−27642

Table 3. continued

(b) *Cm*

Raman mode	ω (cm^{-1})	γ^a	exptl (cm^{-1})	Raman mode	ω (cm^{-1})	γ^a	exptl (cm^{-1})
(A″)	290.11	0.85					
(A′)	290.81	0.90					
(A″)	295.41	1.18					
(A″)	302.70	1.34					

(c) *Cc*

Raman and IR Mode	ω (cm^{-1})	γ^a (0−10 GPa)	γ^c (15−30 GPa)
A′	89.47	2.243	−0.011
A″	105.64	1.962	−0.010
A″	117.32	1.614	0.003
A′	125.65	2.124	0.004
A″	127.67	2.267	0.005
A′	140.38	3.062	0.003
A″	141.75	3.312	0.001
A′	164.50	1.738	0.003
A′	198.25	0.082	0.008
A″	212.84	1.086	0.004
A″	234.43	1.386	0.005
A′	273.18	0.663	0.003
A″	303.12	0.179	0.006
A′	312.33	0.942	0.005
A″	339.78	0.693	−0.003
A′	348.69	0.682	−0.003
A″	398.84	0.964	0.000
A′	422.36	0.609	0.006
A′	471.91	−0.069	0.001
A″	476.98	0.319	0.002
A″	534.46	−0.043	0.003
A″	615.53	0.350	0.002
A′	646.39	0.326	0.003
A′	724.06	0.055	0.000
A″	858.77	0.160	0.000
A′	906.73	−0.233	0.001
A″	948.30	0.284	0.002

(d) *Amm2*

Raman mode	ω (cm^{-1})	γ^a(0−10 GPa)
B_2	105.07	−6.04
B_1	139.41	0.68
A_1	163.67	0.40
B_1	167.76	0.94
A_2	264.19	0.18
B_2	342.56	−1.03
A_1	347.44	−0.26
B_1	409.96	−0.22
A_1	535.96	−0.54
B_2	573.44	0.18
B_1	830.95	−0.20

$^a\gamma = [B_0/\omega_0]\, d\omega/dP$ (0−10 GPa). ^{b}Exp 51. ^{c}Exp 83.

by the *Amm*2 $AgVO_3$ with a volume reduction of about 11.0% over the same range. *Amm*2 EOS parameters, K_0 = 66.82 GPa and K_0' = 4.20, characterize an open structure with an empty space (low electron density) among cations and anions. Its K_0 value lies between that of the monoclinic *C*2/*c* (40.68 GPa [K_0' = 10.45]) and those of the *Cm* and *Cc*−$AgVO_3$ monoclinic structures (118.09 GPa [K_0' = 4.83] and 127.86 GPa [K_0' = 0.86], respectively). The three monoclinic polymorphs (*C*2/*c*, *Cm*, and *Cc*) exhibit noticeable volume reduction of 12.2, 7.0, and 7.5% between 0 and 10 GPa, respectively; meanwhile, the cubic $Pm\bar{3}m$ structure presents higher K_0 and is obviously less compressible and presents a volume reduction, within the same pressure range of 3.9%.

As we can see in Figure1, the three monoclinic and orthorhombic structures present empty volumes that are formed by unoccupied O polyhedra among the [AgOx] and [VOx] occupied clusters. At ambient pressure, B3LYP empty volumes represent 72.7%, 68.8%, 58.4%, and 56.2% of the corresponding optimized unit−cell volumes, for *C*2/*c*, *Amm*2, *Cm*, and *Cc* structures, respectively. This fact can explain the compressibility

DOI: 10.1021/acs.jpcc.7b09865
J. Phys. Chem. C 2017, 121, 27624−27642

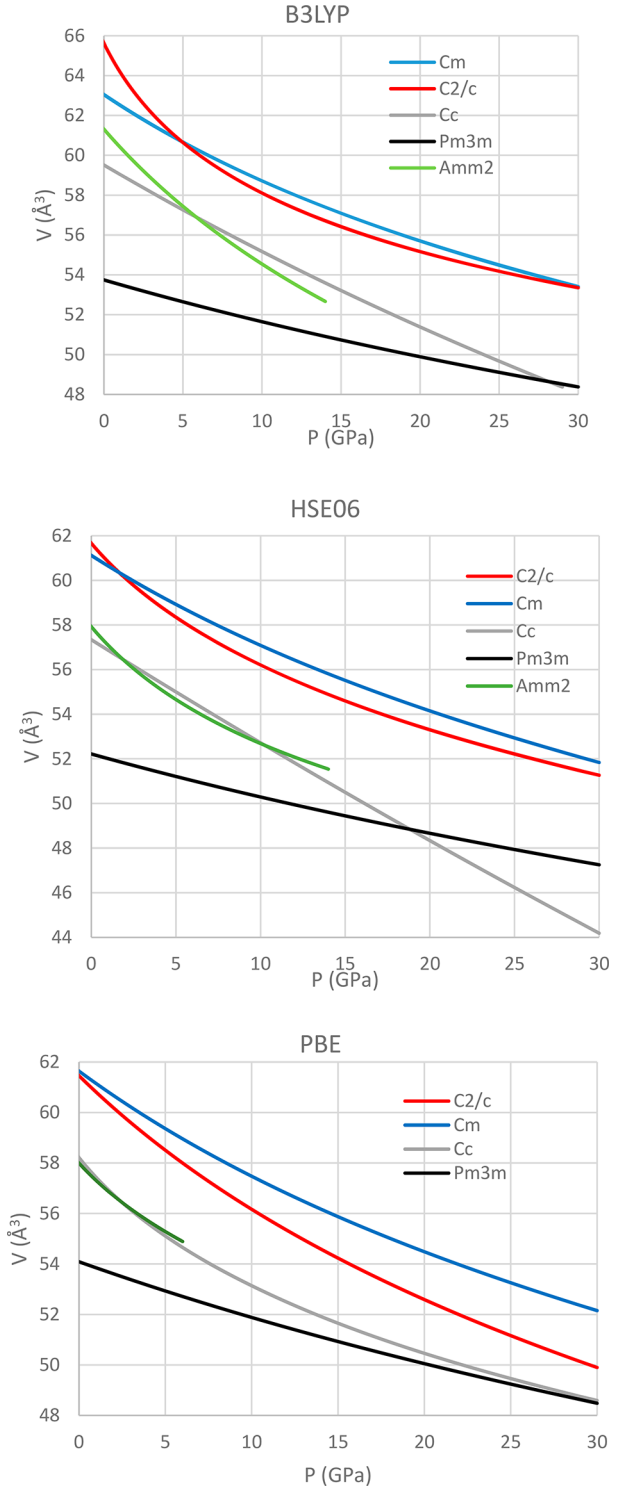

Figure 3. Volume dependence (per unit formula) with pressure of the seven polymorphs calculated with the (a) B3LYP, (b) HSE06, and (c) PBE functionals.

order between the five studied polymorphs as well as the high compressibility that is exhibited, especially by the *C*2/*m* and *Amm*2 polymorphs. On the other hand, the cubic ($Pm\bar{3}m$) polymorph does not present empty space between the occupied polyhedra, and consequently, this structure is less compressible. The corresponding EOS calculated with the HSE06 and PBE can be found in Figure3 (panels b and c, respectively) and Table 1. An analysis of the results shows that both functionals provide different values of the equilibrium volume for the five polymorphs; however, a similar trend is observed in the plot of volume versus pressure. It should be noted that the results, which were obtained at B3LYP and HSEO6 levels, have large values for K_0' (>10) for α- $AgVO_3$. In addition, the *Amm*2 structure also has a large K_0' value at both HSE06 and PBE functionals.

In Figure4 (panels a−e), the behavior of the B3LYP-normalized geometric parameters (a/a_0, b/b_0, c/c_0, and β/β_0) with pressure is depicted from 0 to 30 GPa. In the case of *C*2/*c*-$AgVO_3$, the lattice parameter *b* decreases by about −18% in the 0−30 GPa pressure range, while the *c* and *a* parameters change to a lower extent, by about −6% and −1%, respectively, with respect to the zero−pressure value. Thus, the *b* axis is more compressible than the *a* and *c* directions. This behavior can be associated with the presence of empty space between the $[AgO_6]$ units linked by the $[VO_4]$ polyhedra. Note that the *a* and *c* *C*2/*c*-$AgVO_3$ cell parameters increase, and above 4 GPa, they decrease, whereas the *b* parameter always decreases with pressure (see Figure 4a). The compression along the [010] direction causes a decrease in the parameter *b*, which is due to the presence of unoccupied volume between the $[VO_4]$ polyhedra. This behavior is not possible along the [100] or [001] directions.

In the case of *Cm*-$AgVO_3$, lattice parameters *c* and *a* decrease by about −9% and −8% in the 0−30 GPa pressure range, while *b* changes by less than a −1% (see Figure 4b). In this case, the compression along both [001] and [100] easily reduces the section of the rhombohedral and triangular channels and, consequently, the vacuum space between the occupied polyhedra. The parameter *a* of the monoclinic *Cc*-$AgVO_3$ decreases by −5% with pressure from 0 to 10 GPa, and this decrease is more evident from 10 to 12.5 (an additional −9%), while it is small in the 12.5−30 GPa pressure range (by only −1%). From 0 to 10 GPa, the parameters *b* and *c* remain practically constant, and from 10 to 12.5 GPa, they show an increase of 5% and 6%, respectively. From 12.5 to 30 GPa, decrease of 2% and 3%, are respectively observed (see Figure 4c), with the overall effect being an increase of around 2.4% in both cases. As shown by the decrease of parameter *a*, compression along the [100] direction reduces the vacuum space between the $[AgO_6]$ polyhedra, especially from the pressure at 12.5 GPa. The value of the parameter *a* at the cubic ($Pm\bar{3}m$) structure decreases uniformly about 3%, in the same pressure range (see Figure 4d). The lattice parameter *a* of the orthorhombic (*Amm*2) structure increases by +5% from 0 to 14 GPa and the *b* and *c* parameters decrease uniformly by −9% and −8% from 0 to 14 GPa, respectively (see Figure 4e). In this case, the biaxial compression at the (100) plane is favored, owing to the presence of empty O8 polyhedra between the $[AgO_9]$ and $[VO_4]$ clusters. For the orthorhombic structure, we obtain a very large PBE value for the first pressure derivative of the bulk modulus. Together with the appearance of a negative vibrational frequency at pressures greater than 5 GPa, this suggests that the structure becomes less compressible and unstable above 5 GPa.

The pressure affects the local geometry by changing the interatomic distances and bond angles. In response to pressure, the inorganic framework is modified by the contractions of Ag−O and V−O bond lengths, changes in the O−Ag−O and O−V−O bonding angles, and/or Ag−O−V bridges coupled with the $[AgO_x]$ (x = 4, 5, 6, 7, 9, and 12) and $[VO_x]$ (*x* = 4, 5, and 6) polyhedral tilting. The behavior of the main bonds lengths, V−O and Ag−O, is illustrated in Figure 5. In the $AgVO_3$ structures, the V−O bond is approximately 1.4 times shorter than the Ag−O bond. As expected, for the three monoclinic structures, the mean

DOI: 10.1021/acs.jpcc.7b09865
J. Phys. Chem. C 2017, 121, 27624−27642

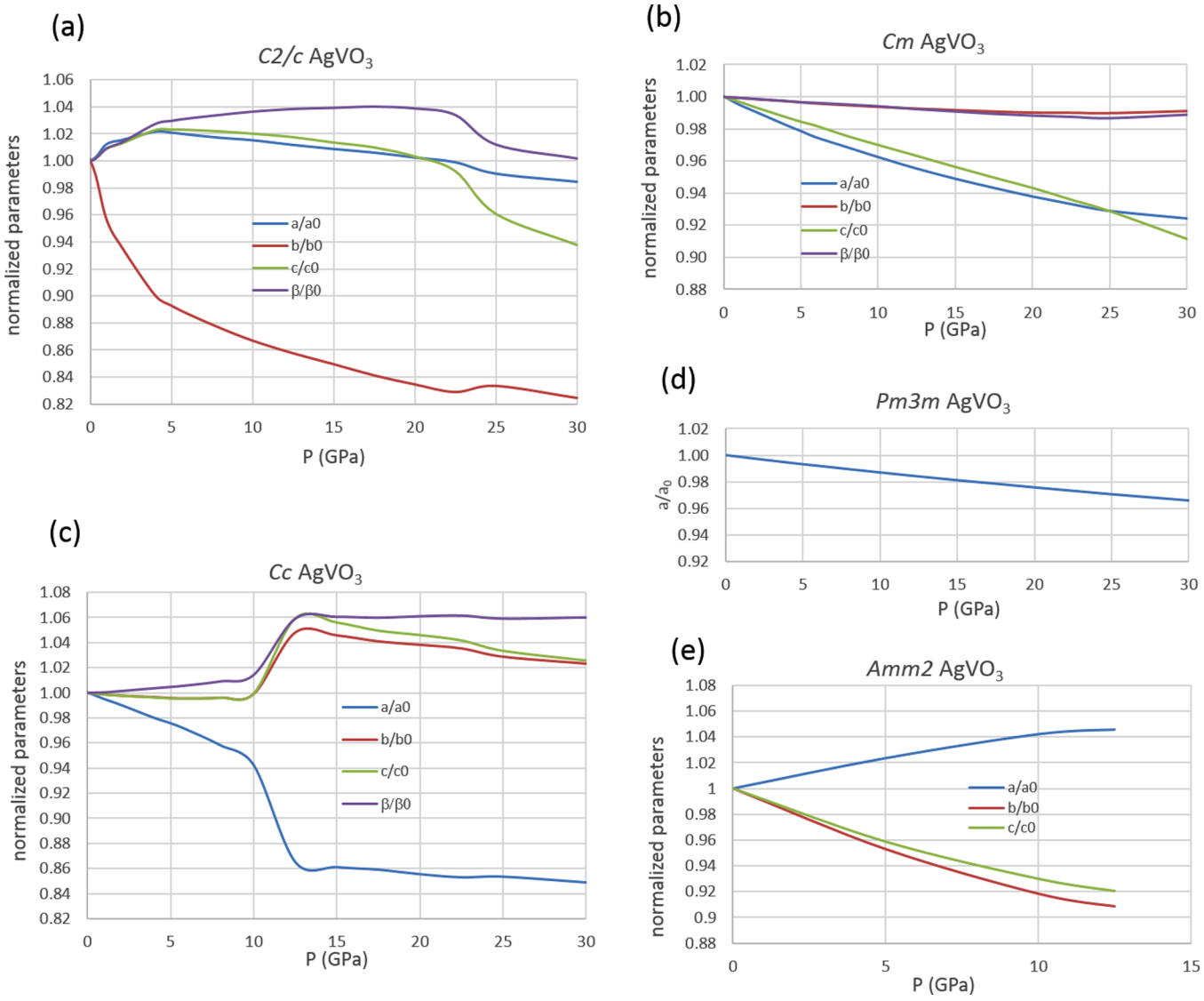

Figure 4. Dependence with pressure of the normalized geometric parameters (a/a_0; b/b_0; c/c_0, and β/β_0): dependence with pressure from 0 up to 30 GPa (a) α-, (b) β-, (c) *Cc*-, (d) cubic $Pm\bar{3}m$-, and (e) from 0 up to 14 GPa for orthorhombic *Amm2*-$AgVO_3$.

Ag−O distances generally decrease by around −6% as the hydrostatic pressure increases in the range from 0 to 30 GPa, and significant reductions of −10% and −8% are observed in mean Ag−O distance for the *Cm* [AgO_7] and *C*2/*c* [AgO_4] polyhedra, respectively. The mean V−O distance shows a reduction of −1.3 and −0.8% in the case of the *C*2/*m* and *Cm* structures, respectively. In the case of the *Cc* structure, the mean V−O distance slightly decreases from 0 to 10 GPa and from 12.5 to 30 GPa but the distance increases from 10 to 12.5 GPa, with a general increase of +1%; at the same time, the mean Ag−O distance in the [AgO_7] cluster shows a large decrease between 10 and 12.5 GPa (see Figure 5a). This behavior as well as the change of the cell parameters versus pressure shown in Figure 4c appear to indicate the presence of a displacive isomorphic phase transition (IPT) at 12.5 GPa, as observed in the abrupt change of the vibrational frequencies between 10 and 15 GPa and the change in the electronic band structure (see next section).

The mean V−O and Ag−O distances of the $Pm\bar{3}m$ and *Amm2* structures are shown in Figure 5b. All of the Ag−O distances decrease as pressure increases. The [VOx] polyhedra are always less compressible than the [AgOx] ones; the mean V−O distance slightly decreases in the cubic ($Pm\bar{3}m$) (−3.4%) structure and remains practically constant (from 0 to 14 GPa) in the orthorhombic (*Amm2*) (+0.7%) structure. The Ag−O bonds decrease by around −3.5% in the cubic ($Pm\bar{3}m$) structure and by −3.2% (from 0 to 14 GPa) in the orthorhombic (*Amm2*) polymorph.

Overall, our results indicate that the different response of the $AgVO_3$ polymorphs under hydrostatic pressure can be associated with a specific anisotropy in terms of the structure for each polymorph. B3LYP calculations give the following compressibility order of the different polymorphs *C*2/*c* > *Amm2* > *Cm* > *Cc* > $Pm\bar{3}m$, owing to the presence of a larger empty volume among the occupied polyhedra (i.e., [AgOx] and [VOx] clusters). This order is obviously the same as reflected by the values of the corresponding bulk modulus shown in Table 1. HSE06 and PBE calculations show that the cubic structure is also less compressible, but they both give different compressibility orders (i.e., *Amm2* > *C*2/*c* > *Cc* > *Cm* > $Pm\bar{3}m$), with *Amm2* being the most compressible structure. The difference is in the compressibility of both *Cc* and *Cm* polymorphs, and this change may be associated with the fact that the EOS *Cc* polymorph, at

DOI: 10.1021/acs.jpcc.7b09865
J. Phys. Chem. C 2017, 121, 27624−27642

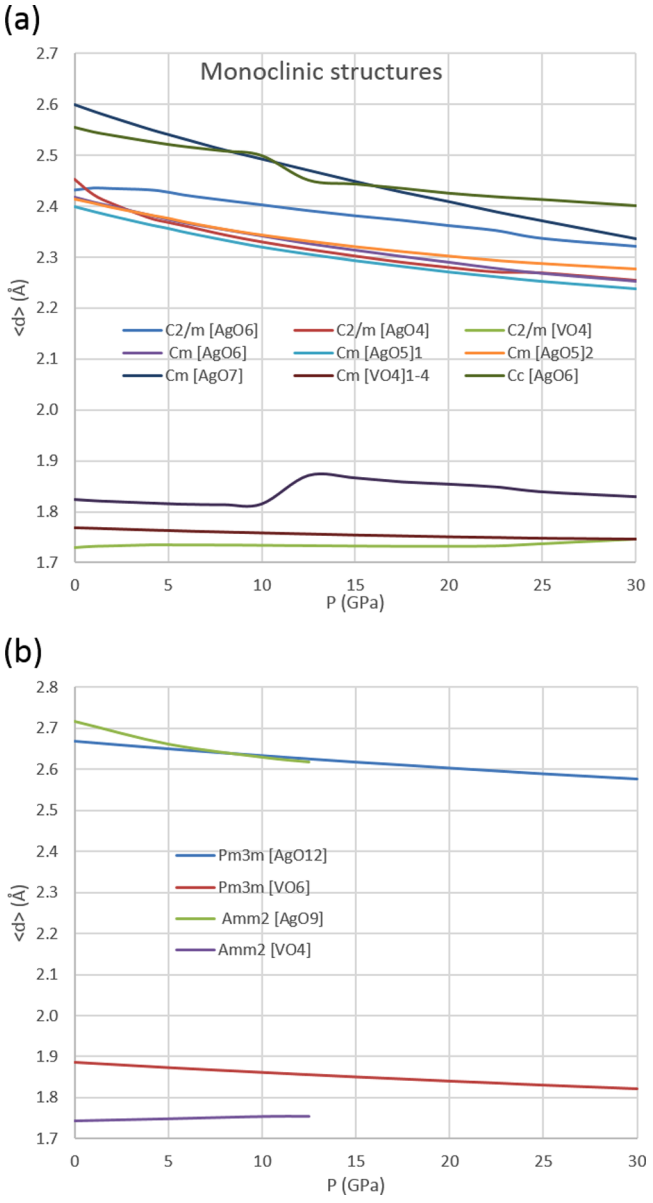

Figure 5. Behavior of the main bonds lengths, V−O and Ag−O, with pressure for (a) monoclinic polymorphs and (b) for $Pm\bar{3}m$ and *Amm2* structures.

the B3LYP and HSE06 levels, displays an unusually low value for K_0', ($K_0'<1$), whereas the *Cm* polymorph has more standard values of K_0', ($K_0' \sim 4$),

In addition to structural data, vibrational stretching frequencies were calculated in order to determine their correlation with V−O and Ag−O bond lengths as well as the charge transferred. To this end, we employed the Badger's rule[84] to analyze the presence of electron charge processes along with the compression of different polymorphs. This rule states that the strength of a bond correlates with the frequency (ω) of its vibrational mode, $\omega = A/(r_{MO} - B)^{3/2}$, where A and B are constants and r_{MO} the metal−oxygen distance. If this rule is followed by the breathing or stretching vibrational modes of the [AgO_x] and [VO_x] clusters, we can assert that the behavior of the frequencies with pressure is due only to geometrical factors, while if the rule is not fulfilled, charge transfer or other factors are involved.

The *Cm*−$AgVO_3$ presents breathing modes for the four types of [VO_4] polyhedra and two combined stretching and bending modes for the [AgO_6] and [AgO_5] ones. As pressure is applied, the variation of the Ag−O and V−O distances follows the Badger's rule.

For cubic $Pm\bar{3}m$−$AgVO_3$, there is only an IR active mode (F1u) owing to the breathing of [VO_6] clusters. The [VO_6] clusters follow the Badger's rule, whereas the mechanical effect of the applied pressure is the dominant factor that leads to a shortening of Ag−O and V−O distances.

3.4. Energetics. The calculated values for the pressure of the phase transition among the five polymorphs are summarized in Table 4. In order to study the energetic stability of the selected

Table 4. Calculated Pressure Transitions between the Five Studied $AgVO_3$ Polymorphs with the B3LYP, HSE06, and PBE Functionals

	P_T (GPa)				
	Cm to *Cc*	*Cm* to *Amm2*	*Cm* to $Pm\bar{3}m$	*C2/c* to $Pm\bar{3}m$	*Cm* to *C2/c*
B3LYP	5	8	22	19	–
HSE06	3	5	18	15	–
PBE	2	5	15	11	23

phases of $AgVO_3$ under high pressure, we plotted the variation of total energy, E, as a function of volume, and the relative enthalpy−pressure ($\Delta H-P$) curves for each phase relative to the β phase, as shown in Figures 6 and 7 for the five polymorphs.

An analysis of the results of Figure 7 and Table 4 shows that the values of pressure for the phase transition are dependent on the functional used. The minimum enthalpy path involves one transition phase along *Cm*−*Cc*, at 5 GPa, at the B3LYP level, while for both HSE06 and PBE functionals, the transition between *Cm* and *Cc* polymorphs, takes place at 3 and 2 GPa, respectively.

Note that the orthorhombic (*Amm2*) structure at the B3LYP level exceeds 8 GPa and is more stable than *Cm*-$AgVO_3$. For the HSE06 and the PBE functionals, the *Amm2* structure is more stable than the *Cm*-$AgVO_3$ above 5 GPa with both functionals and it always has a greater enthalpy than the *Cc* structure for the three functionals used in this work.

Figure 7a shows that the monoclinic *Cc*-$AgVO_3$ structure becomes the most stable above 5 GPa and at 5 GPa, which is a decrease of volume (−5.5%), 3.38 $Å^3$, and can be observed with respect to β-$AgVO_3$ (see Figure 3a).

The analysis of the B3LYP results shows that the cubic polymorph becomes more stable than *C2/c*− and *Cm*−$AgVO_3$ at 19 and 22 GPa, respectively. No pressure-induced transition was found between the *C2/c*− and *Cm*−monoclinic $AgVO_3$. The difference between the pressures of the phase transition of *Cm*−$AgVO_3$ into the *Cc* phase, which is calculated with a different functional, is up to 5 GPa (B3LYP), 3 GPa (HSE06), and 2 GPa (PBE). The calculated HSE06 transition pressures of *C2/c*− and *Cm*−$AgVO_3$ into the cubic $Pm\bar{3}m$ phase are 15 and 18 GPa, respectively, whereas the corresponding PBE values are 11 and 15 GPa, respectively (see Table 4).

The $Pm\bar{3}m$ phase is the least compressible polymorphs. This structure does not present unoccupied polyhedra. The *Amm2* polymorph presents an unoccupied volume of 68.8%, and it shows the largest relative stabilization with respect to other polymorphs up to a pressure of 14 GPa. There are several breathing modes but only for the [VO_4] clusters [i.e., 830.9 cm^{-1}

DOI: 10.1021/acs.jpcc.7b09865
J. Phys. Chem. C 2017, 121, 27624−27642

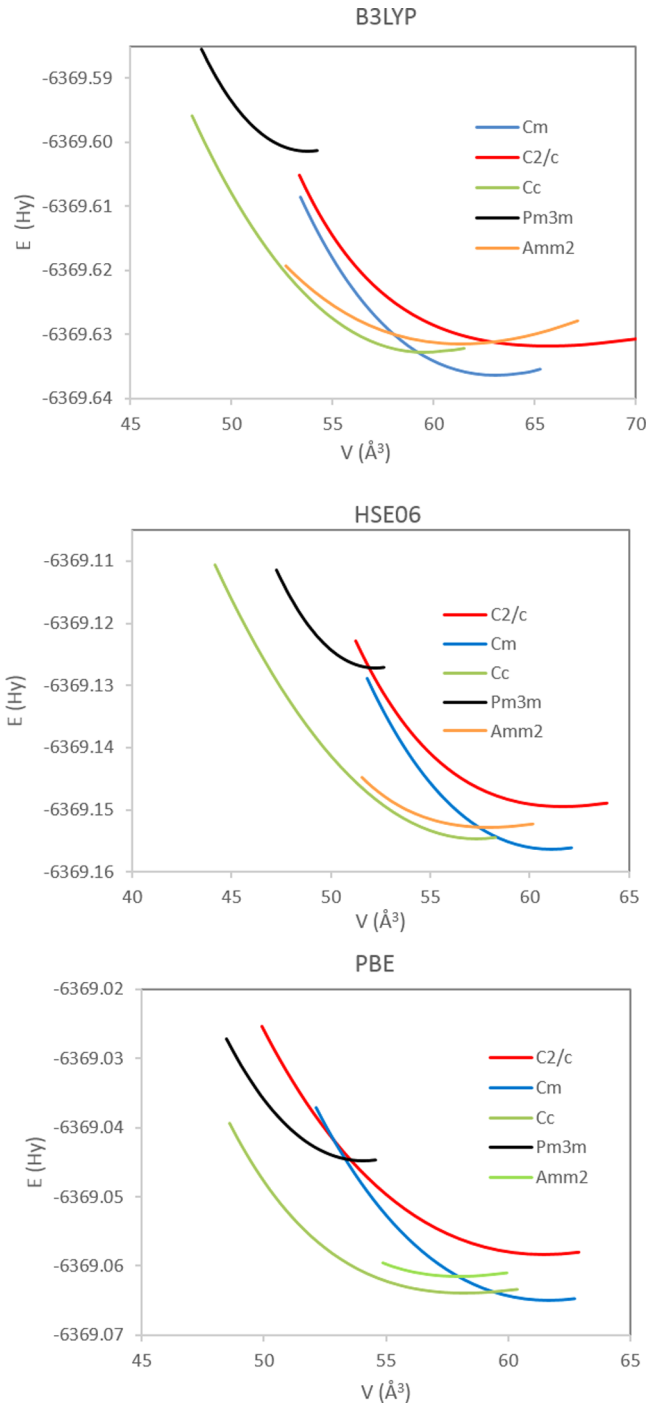

Figure 6. Total energy vs volume for the seven $AgVO_3$ polymorphs calculated with the (A) B3LYP, (b) HSE06, and (c) PBE functionals.

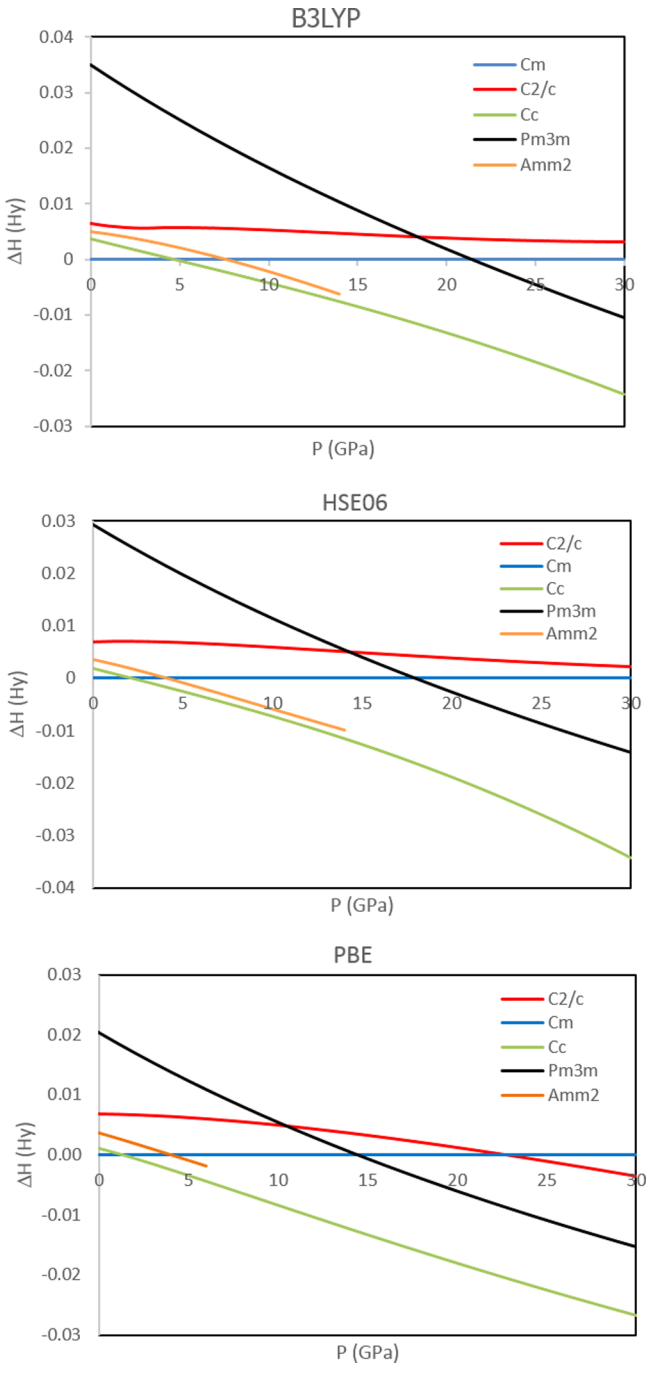

Figure 7. Variation in enthalpy vs pressure (with the β structure as a reference) for the $AgVO_3$ polymorphs calculated with the (A) B3LYP, (b) HSE06, and (c) PBE functionals.

(B_1) and 919.4 cm^{-1} (A_1) at ambient pressure] that follow the Badger's rule; therefore, the relative stabilization of this structure up to 14 GPa is also due to structural factors. The *Cc*− structure with an unoccupied volume of 56.2% also shows good stabilization as pressure is applied. Only the [VO_5] polyhedra present breathing modes [i.e., 615.53 (A″) and 646.39 (A′) cm^{-1} at ambient pressure], which do not follow the Badger's rule, and the stabilization of this structure is due mainly to electronic factors (see the next section). However, the *C*2/*c* structure has the greatest empty volume (72.7%) and is more compressible. In this polymorph, there are breathing modes for the [VO_4] clusters [i.e., 937 cm^{-1} (Ag)] and stretching modes for the [AgO_6] clusters [i.e., 226 cm^{-1} (Bg)]. The breathing modes of the [VO_5] clusters and the stretching modes of the two [AgO_6] clusters do not follow the Badger's rule.

Table 5 shows the calculated B3LYP values for variations of enthalpy, $\Delta_r H$ at zero pressure and temperature for the investigated reactive channels. At zero pressure, the analysis of our results shows that all channels have $\Delta_r H$ positive values, and the reactive channel: $4AgVO_3 \rightarrow Ag_2V_4O_{11} + Ag_2O$ presents the lower value of ΔH (0.41 eV) and ΔV (1.58 $Å^3$) of all the investigated reactive channels (the values are with reference to a unit formula of $AgVO_3$). Calculations also show that the $AgVO_3$ decomposition process into their constituent oxides V_2O_5 and

DOI: 10.1021/acs.jpcc.7b09865
J. Phys. Chem. C 2017, 121, 27624−27642

Table 5. Calculated B3LYP Values of the Reaction Enthalpy, $\Delta_r H$, for the Different Reactive Channels of $AgVO_3$ Studied and the Corresponding Volume Variation, $\Delta_r V$

dissociation channel	$\Delta_r H$ (eV)	$\Delta_r V$ (Å^3)
$AgVO_3 \rightarrow Ag_2O + V_2O_5$	1.03	9.80
$AgVO_3 \rightarrow AgO + VO_2$	2.42	−4.86
$AgVO_3 \rightarrow Ag + V + \frac{3}{2}O_2$	7.21	–
$AgVO_3 \rightarrow \frac{1}{4}Ag_4V_2O_7 + \frac{1}{4}V_2O_5$	11.13	3.84
$AgVO_3 \rightarrow \frac{1}{4}Ag_2V_4O_{11} + \frac{1}{4}Ag_2O$	0.41	1.58

Ag_2O are not energetically favorable, having positive values (1.03 eV) and ΔV (9.80 Å^3) at zero pressure; the other processes studied have greater reaction enthalpies. Therefore, for these two reactions with lower enthalpies, we studied the stability of $AgVO_3$ versus that of $Ag_2V_4O_{11}$ and Ag_2O and against binary oxides at different pressures. With an increase of pressure, ΔH (not shown in Figure 7) and ΔV values of these reactive processes are always positive.

Calculations with HSE06 and PBE functionals show the same behavior as those that were performed using the B3LYP functional.

3.5. Electronic Properties. A high pressure is capable of modulating the electronic structure, as with the density of state (DOS) and energy gap. The resultant DOS and band gap depend on the contributions of the competitive structural pressure effects, such as the shortening of Ag−O and V−O bonds as well as the Ag−O−Ag and V−O−V angle bending.

The calculated B3LYP band structures, as well as the DOS projected on atoms at ambient pressure, are displayed in Figure 8. The analysis of the band structures indicates that α- and β-$AgVO_3$ present an indirect band gap from A (1/2,0,0) and a point near M (1/2,1/2,1/2), whereas the *Cc* structure has a direct band gap at Γ; however, at pressures greater than 12.5 GPa, it becomes indirect from the point (1/4,0,0) near A (1/2,0,0) and Γ. The DOS of the three monoclinic polymorphs indicates that the upper part of the valence band (VB) consists of noninteracting Ag 4d and O 2p orbitals, and a high contribution of 3d V and Ag 5s orbitals are observed in the lower part of the conduction band (CB). The cubic $Pm\bar{3}m$ structure presents an indirect band gap from Γ to X (0, 1/2,0), and the orthorhombic *Amm2* structure presents an indirect band gap from T (1/2,1/2,1/2) to Γ and here too the upper VB consists mainly of Ag 4d and O 2p orbitals and of 3d V orbitals in the lower CB in both cases. The values of the band gap energies (E_g) at ambient pressure calculated with the three functionals as well as the available experimental data are shown in Table 6. The B3LYP and HSE06 band gap energies are larger than experimental values, whereas the PBE functional underestimates the band gap; these differences between calculations and experiments are typical of DFT calculations.

At ambient pressure, all of the structures studied present indirect band gaps, except for the *Cc* monoclinic polymorph, which shows a direct band, and the minimum E_g values follow the sequence *Amm2* > *C2/c* > *Cm* > *Cc* > $Pm\bar{3}m$.

The hydrostatic band gap deformation potential,[86] a_g, can be defined as the product of the bulk modulus and the variation of the band gap with pressure $a_g = K_0 \frac{dE_g}{dP}$. Figure 9 shows the pressure dependence of the indirect band gap E_g for the five polymorphs up to 30 GPa; that is *Amm2*, *C2/c*, and *Cm* cases decrease with pressure, having their hydrostatic band gap deformation potentials of −5.07, −2.62, and −2.49 eV, respectively. The indirect gap of the *Cc* polymorph decreases from 12.5 up to 30 GPa. In Figure 9, we also represent the direct gap of the *Cc* structure from ambient to 10 GPa using a dotted line. The E_g of the cubic polymorph remains practically constant around 0.9 eV at all pressures and its a_g is equal to −0.04 eV.

Between ambient pressure and 10 GPa, the E_g of the *Cc* structure is direct at Γ and decreases from 2.92 to 2.83 eV; however, from 12.5 GPa up to 30 GPa, it becomes indirect from Γ to A and jumps to 3.92 eV at 12.5 GPa, while it decreases to 2.93 eV at 30 GPa. The corresponding values of a_g are −1.26 eV from ambient to 10 GPa and −1.97 eV from 12.5 to 30 GPa. This may be related to the behavior of the cell parameters when the pressure increases from 10 to 12.5 GPa (i.e., parameter *a* decreases by −9%, whereas *b* and *c* show increases of 5% and 6%, respectively).

The same relative pressure dependences are found for HSE06 and PBE, and the primary difference is that in the cubic case, the PBE calculations renders a conductor state; this is in agreement with previous theoretical PBE calculations reported by Al-Zaghayer et al.[50]

In order to evaluate the influence of the electronic factors on the pressure behavior of the different structures, we calculated the atomic Mulliken charges, focusing mainly on the monoclinic *C2/c* and *Cc* polymorphs. The choice of the Mulliken partition is arbitrary because there is no unique method of performing the partition of the charge density. However, the choice of the given scheme remains extremely useful when comparing the results of calculations performed using similar basis sets.[87]

Figure 10 (panels a and b) shows the pressure dependence of the variation of the Mulliken atomic charges of the Ag, V, and oxygen atoms with respect to their values at zero pressure, for (a) *C2/c*- and (c) *Cc*-$AgVO_3$, respectively. In Figure 10 (panels c and d), the Mulliken charges for the oxygen atoms of both polymorphs are presented. An analysis of the results shows that for *C2/c*-$AgVO_3$ and *Cc*-$AgVO_3$ structures, a noticeable charge transfer takes place from the Ag and V cations to the O2 anions (0.14 e-) and O1 anions (0.14 e-), respectively, when an external pressure is applied, in the range of 0−30 GPa. This behavior explain why the Badger's rule is not followed in these two polymorphs. Small variations in the values of Mulliken charge with pressure are sensed at the Ag and V cations and O anions of the *Cm*, *Amm2*, and $Pm\bar{3}m$ polymorphs; therefore, the Badger's rule is fulfilled (see Figure S2), showing the prevalence of the geometrical factors.

4. CONCLUSIONS

Pressure is a versatile thermodynamic parameter that can be exploited in the pursuit of new materials. Polymorphism opens up the possibility of fine-tuning crystal packing without changing the chemical structure and offers a new avenue for optimizing device performance. For many technological applications, it is necessary to find more details from their different phases and their transformations induced by pressure. A specific rate of pressure increase may trigger unexpected solid-state transformations, producing otherwise inaccessible phases. High-pressure polymorphs of complex oxides are of interest because of their ability to produce unique geometries and electronic structures with different bonding environments with respect to the stable phase in ambient conditions.

This work is part of an ongoing study by our research group, which is focused on the theoretical study of the properties of solid materials under the influence of pressure. To the best of our knowledge, there have been no studies on the high-pressure

DOI: 10.1021/acs.jpcc.7b09865
J. Phys. Chem. C 2017, 121, 27624−27642

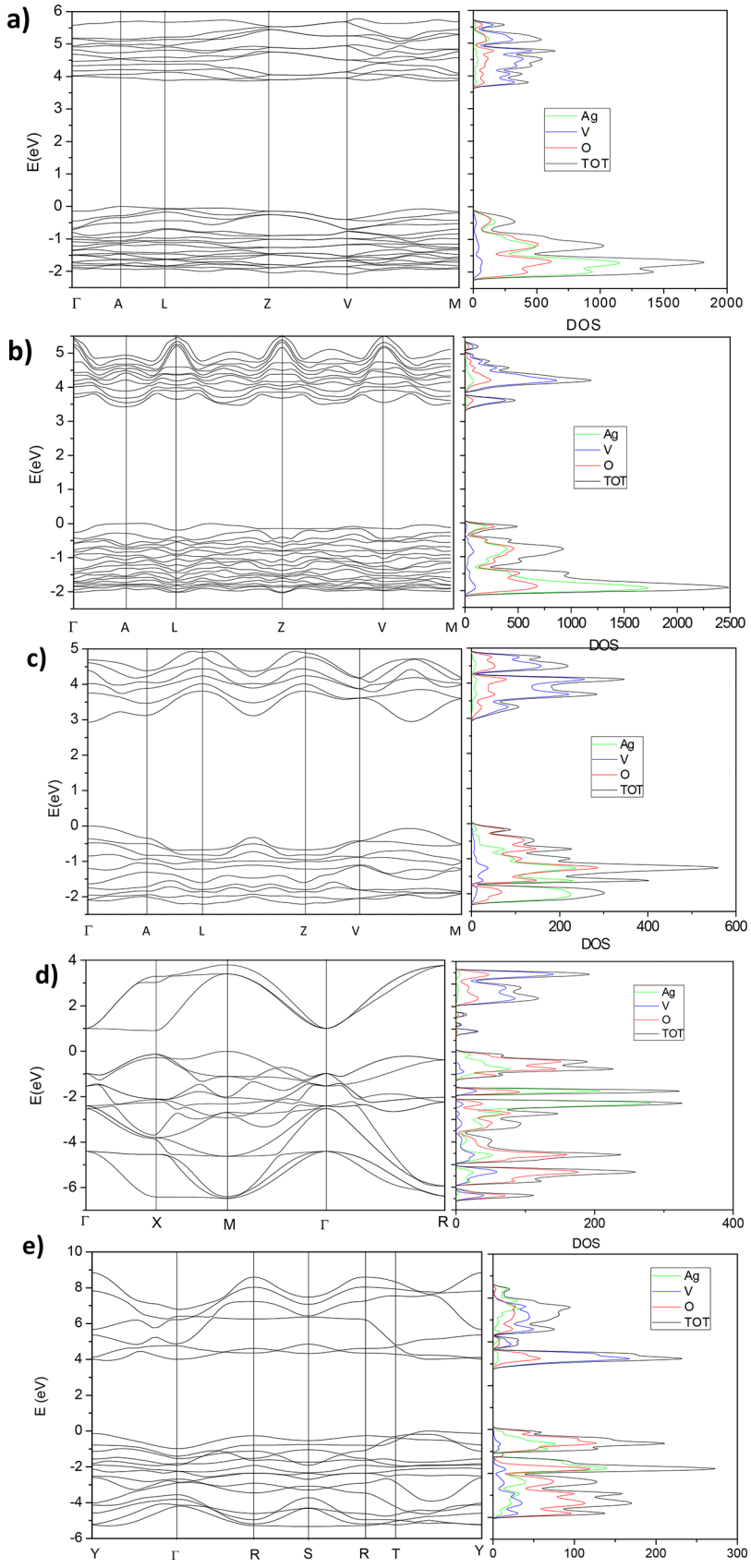

Figure 8. Calculated B3LYP band structures and the DOS projected on atoms for (a) α-$AgVO_3$, (b) β-$AgVO_3$, (c) *Cc*-$AgVO_3$, (d) $Pm\bar{3}m$-$AgVO_3$, and (e) *Amm2*-$AgVO_3$.

behavior of $AgVO_3$ type structures. Here, we have performed a comprehensive analysis of the structural and electronic properties of silver vanadium oxide ($AgVO_3$) in five phases as a function of the pressure. The present investigation provides new

DOI: 10.1021/acs.jpcc.7b09865
J. Phys. Chem. C 2017, 121, 27624−27642

Table 6. Calculated B3LYP, HSE0, and PBE Values of the Indirect and Direct Band Gap, E_g, in eV, Together with the Experimental Values for α- and β-$AgVO_3$

		exptl	B3LYP	HSE06	PBE
α ($C2/c$)	E_g (A→~M)	2.5[85]	3.81	3.44	1.80
	E_g(Γ)		4.15	3.68	2.08
β (Cm)	E_g(A→~M)	2.0[39,41]	3.43	3.19	1.60
	E_g(Γ)		3.97	3.72	2.03
Cc	E_g(Γ)		2.93	2.60	1.26
$Pm\bar{3}m$	E_g(M → X)		0.90	0.64	conductor
	E_g(Γ)		1.98	1.98	
$Amm2$	E_g(T→Γ)		3.92	3.39	1.68
	E_g(Γ)		4.99	4.49	2.66

structural, electronic, vibrational, and optical results from first-principles calculations, using B3LYP, HSE06, and PBE functionals within the framework of DFT, to predict structural and thermodynamic properties and to examine solid-state transformations of $AgVO_3$ polymorphs, which are not yet experimentally known. As the energetic separation and the structural differences between the phases are small and thus potentially sensitive to aspects of the computational procedure, we have placed special emphasis on the influence of different approximations on the exchange-correlation functional. To the best of our knowledge, most of the properties studied here have not been previously reported; however, these results need to be confirmed by performing experiments.

The main conclusions of present of our work can be summarized as follows: (i) five different bulk phases, monoclinic (α, β, and Cc)-orthorhombic ($Amm2$) and cubic ($Pm\bar{3}m$) perovskite-type structures, have been characterized, and the nature of their pressure-induced structural changes have been analyzed. Therefore, new polymorphs of monoclinic-type $AgVO_3$ with a space group Cc structure, orthorhombic, and cubic phases are proposed. (ii) The first phase transition between β-$AgVO_3$ and the new and previously unreported Cc phase, which was calculated using different functionals, is up to 5 GPa (B3LYP), 3 GPa (HSE06), and 2 GPa (PBE). (iii) Pressure-induced transitions are found between the β-, α-monoclinic and cubic structures, and the corresponding values for the pressure transitions are dependent on the functional used. (iv) Vibrational frequency values as well as their pressure dependence for monoclinic (α, β, and Cc)-$Amm2$ and cubic−$AgVO_3$ structures were obtained. (v) On the basis of quantum chemical simulations, we presented the energetics of the reactive channels from $AgVO_3$ to Ag_2O and V_2O_5, to AgO and VO_2 mixtures, to silver pyrovanadate, $Ag_4V_2O_7$, and V_2O_5, to $Ag_2V_4O_{11}$ and Ag_2O structures, as well as to O2, V, and Ag. Theoretical results show that the studied reactive channels of β-$AgVO_3$ are not thermodynamically favorable process routes at pressures up to 30 GPa. (vi) All of the structures studied present indirect band gaps, with the exception of the Cc monoclinic polymorph, which shows a direct band from ambient to 12.5 GPa. At ambient pressure, the E_g values follow the sequence $Amm2 > C2/c > Cm > Cc > Pm\bar{3}m$ and decrease in the three first cases with pressure. The E_g Cc structure increases with pressure, whereas the E_g of the cubic polymorph remains practically constant at all pressures. In the three monoclinic polymorphs, the upper part of VB consists of Ag 4d and O 2p orbitals, and the lower part of CB presents a high contribution of 3d V and Ag 5s orbitals. In the cubic and orthorhombic structures, the upper VB also consists of Ag 4d and O 2p orbitals, and the lower CB consists only of 3d V orbitals in both cases. (vii) An analysis of the pressure evolution of geometric, vibrational, and electronic properties of the proposed Cc-$AgVO_3$ monoclinic polymorph indicates that an IPS takes

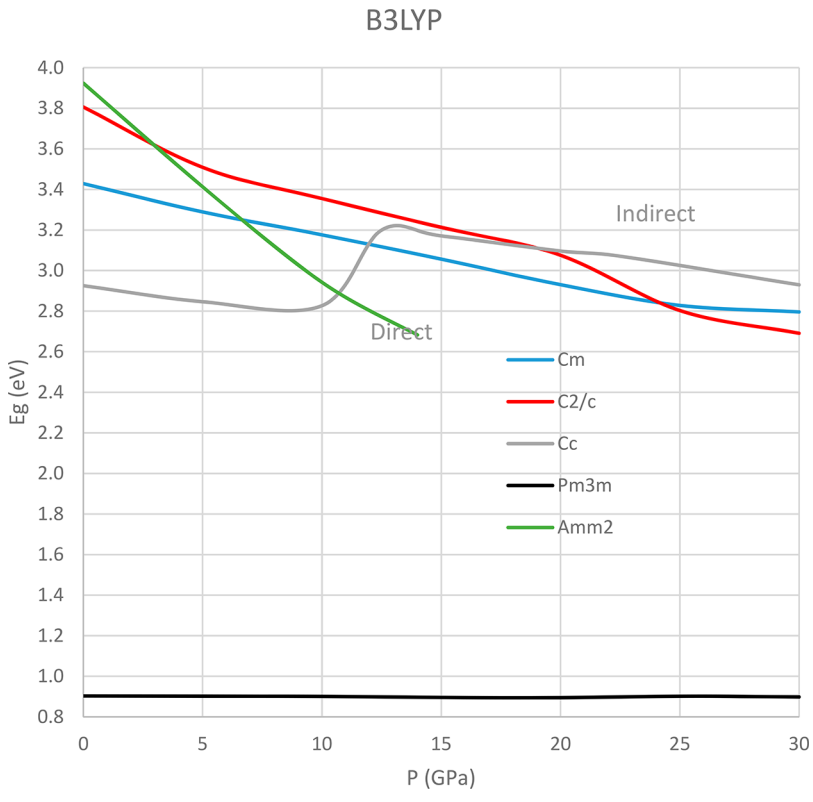

Figure 9. B3LYP E_g dependence on pressure for the five $AgVO_3$ polymorphs.

DOI: 10.1021/acs.jpcc.7b09865
J. Phys. Chem. C 2017, 121, 27624−27642

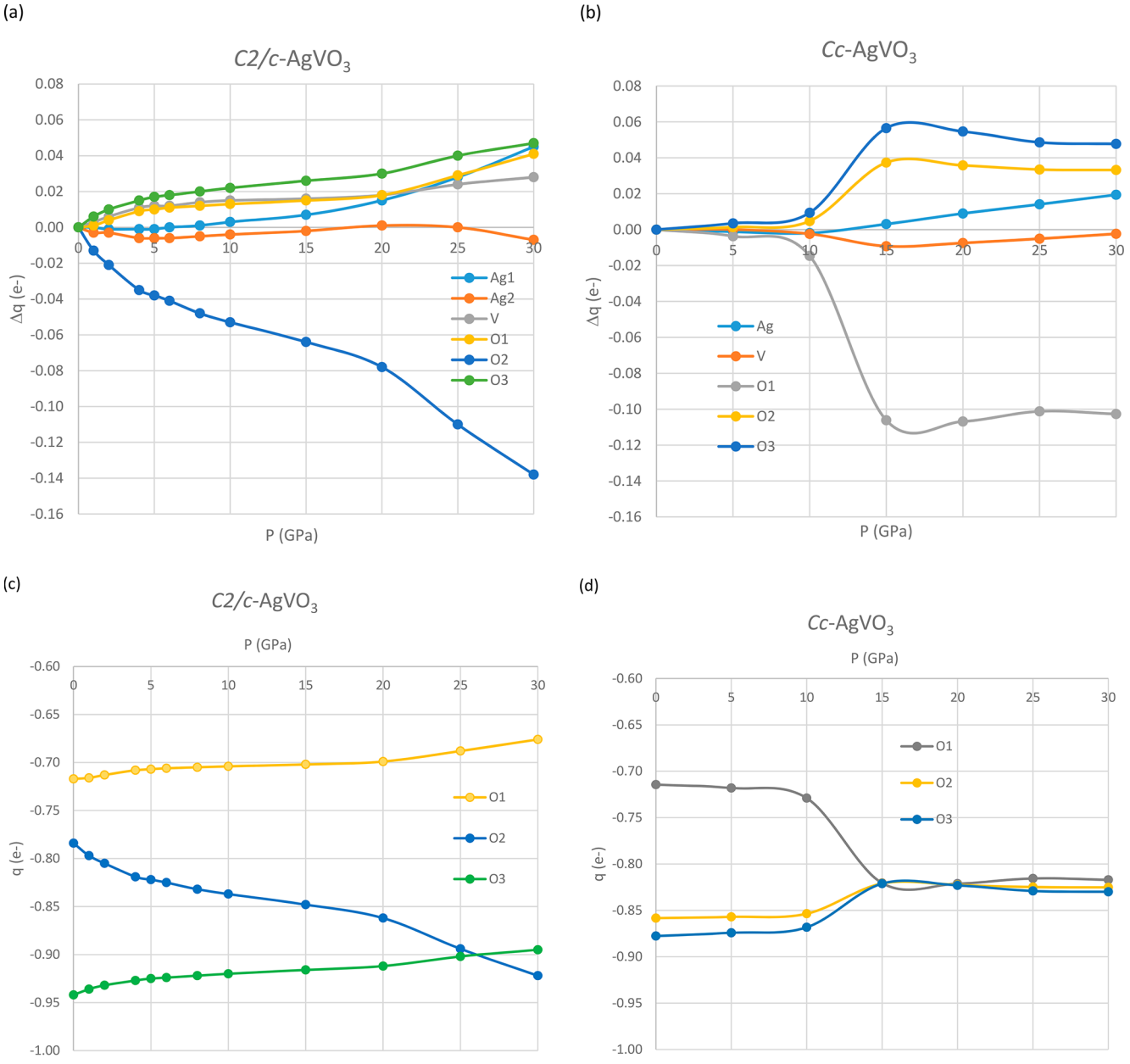

Figure 10. Pressure dependence of the variation of the Mulliken atomic charges (Δq, in e-) of Ag, V, and O, with respect to their values at zero pressure, for (a) $C2/c$-$AgVO_3$ and (b) Cc-$AgVO_3$ structures, and (c) the absolute Mulliken charges of the oxygen atoms for both polymorphs (d) y.

place around 12.5 GPa. (viii) We analyze the variations of different vibrational frequencies and V−O and Ag−O bond lengths as pressure is applied, and the results confirm that Badger's rule is fulfilled for Cm, $Amm2$, and $Pm\bar{3}m$ polymorphs, while the Badger's linear relationships were not found for the $C2/c$ and Cc phases.

In the case of $AgVO_3$, to date, there are no experimental reports on their behavior under pressure. We hope that our study will further motivate theoretical and experimental studies of $AgVO_3$ to further examine and confirm the high-pressure behavior of $AgVO_3$-type structures found in this work and to interpret their different phases as well as their properties under pressure. The findings reported here indicate that the method used to predict relative phase stabilities should be chosen carefully, and that the results should be scrutinized critically. The present study underscores the importance of validating DFT calculations, either by comparison using measurements or, when such results are unavailable, by verifying the accuracy of the exchange-correlation functional that is being used. This is especially important for extreme compressions when interactions between strongly localized semicore electronic states begin to play a role.

■ ASSOCIATED CONTENT

Supporting Information

The Supporting Information is available free of charge on the ACS Publications website at DOI: 10.1021/acs.jpcc.7b09865.

Optimization details, structure of the tetragonal and hexagonal polymorphs, bulk structures, and pressure dependence of the variation of the Mulliken atomic charges (PDF)

DOI: 10.1021/acs.jpcc.7b09865
J. Phys. Chem. C 2017, 121, 27624−27642

AUTHOR INFORMATION

Corresponding Author

*E-mail: Lourdes.Gracia@uv.es.

ORCID

Lourdes Gracia: 0000-0001-9684-2568

Juan Andrés: 0000-0003-0232-3957

Notes

The authors declare no competing financial interest.

ACKNOWLEDGMENTS

The authors acknowledge Generalitat Valenciana for *PrometeoII*/2014/022, ACOMP/2014/270, and ACOMP/2015/1202, and Ministerio de Economía y Competitividad (Spain) for project CTQ2015-65207-P, for financially supporting this research. This work was also supported by Spanish MALTA-Consolider Ingenio 2010 Program (Project CSD2007-00045). J.A. is also grateful to Programa de Cooperación Científica. con Iberoamerica (Brasil) of Ministerio de Educación (Spanish Brazilian program PHBP14-00020), and Ministerio de Economia y Competitividad, "Salvador Madariaga" program, PRX15/00261.

REFERENCES

(1) Starkweather, H. W. Polymerization under high pressure. *J. Am. Chem. Soc.* **1934**, *56*, 1870.

(2) Schettino, V.; Bini, R.; Ceppatelli, M.; Ciabini, L.; Citroni, M. Chemical Reactions at very high pressure. *Advances in Chemical Physics* **2005**, *131*, 105.

(3) Bini, R. Laser-assisted high-pressure chemical reactions. *Acc. Chem. Res.* **2004**, *37*, 95.

(4) Eremets, M. I.; Gregoryanz, E. A.; Struzhkin, V. V.; Mao, H. K.; Hemley, R. J.; Mulders, N.; Zimmerman, N. M. Electrical conductivity of xenon at megabar pressures. *Phys. Rev. Lett.* **2000**, *85*, 2797.

(5) Li, Q. J.; Liu, B. B.; Wang, L.; Li, D. M.; Liu, R.; Zou, B.; Cui, T.; Zou, G. T.; Meng, Y.; Mao, H. K.; Liu, Z. X.; Liu, J.; Li, J. X. Pressure-Induced Amorphization and Polyamorphism in One-Dimensional Single-Crystal TiO2 Nanomaterials. *J. Phys. Chem. Lett.* **2010**, *1*, 309.

(6) Liu, D. D.; Yao, M. G.; Wang, L.; Li, Q. J.; Cui, W.; Liu, B.; Liu, R.; Zou, B.; Cui, T.; Liu, B. B.; Liu, J.; Sundqvist, B.; Wagberg, T. Pressure-Induced Phase Transitions of C-70 Nanotubes. *J. Phys. Chem. C* **2011**, *115*, 8918.

(7) Lu, X. J.; Yang, W. G.; Quan, Z. W.; Lin, T. Q.; Bai, L. G.; Wang, L.; Huang, F. Q.; Zhao, Y. S. Enhanced Electron Transport in Nb-Doped TiO2 Nanoparticles via Pressure-Induced Phase Transitions. *J. Am. Chem. Soc.* **2014**, *136*, 419.

(8) Sanloup, C.; Gregoryanz, E.; Degtyareva, O.; Hanfland, M. Structural transition in compressed amorphous sulfur. *Phys. Rev. Lett.* **2008**, *100*, 10.1103/PhysRevLett.100.075701.

(9) Santoro, M.; Gorelli, F. A.; Bini, R.; Ruocco, G.; Scandolo, S.; Crichton, W. A. Amorphous silica-like carbon dioxide. *Nature* **2006**, *441*, 857.

(10) Sun, Z. M.; Zhou, J.; Pan, Y. C.; Song, Z. T.; Mao, H. K.; Ahuja, R. Pressure-induced reversible amorphization and an amorphous-amorphous transition in Ge2Sb2Te5 phase-change memory material. *Proc. Natl. Acad. Sci. U. S. A.* **2011**, *108*, 10410.

(11) Ballaran, T. B.; Kurnosov, A.; Trots, D. Single-crystal X-ray diffraction at extreme conditions: a review. *High Pressure Res.* **2013**, *33*, 453.

(12) Grochala, W.; Hoffmann, R.; Feng, J.; Ashcroft, N. W. The Chemical Imagination at Work in Very Tight Places. *Angew. Chem., Int. Ed.* **2007**, *46*, 3620.

(13) Klug, D. D.; Yao, Y. Metallization of solid hydrogen: the challenge and possible solutions. *Phys. Chem. Chem. Phys.* **2011**, *13*, 16999.

(14) Lee, R.; Howard, J. A. K.; Probert, M. R.; Steed, J. W. Structure of organic solids at low temperature and high pressure. *Chem. Soc. Rev.* **2014**, *43*, 4300.

(15) Manaa, M. R.; Fried, L. E.; Sabin, J. R. The Reactivity of Energetic Materials Under High Pressure and Temperature. In *Energetic Materials*; Advances in Quantum Chemistry; Elsevier, 2014; Vol. *69*, p 22110.1016/B978-0-12-800345-9.00006-4.

(16) Guillaume, C. L.; Gregoryanz, E.; Degtyareva, O.; McMahon, M. I.; Hanfland, M.; Evans, S.; Guthrie, M.; Sinogeikin, S. V.; Mao, H. K. Cold melting and solid structures of dense lithium. *Nat. Phys.* **2011**, *7*, 211.

(17) Machon, D.; Meersman, F.; Wilding, M. C.; Wilson, M.; McMillan, P. F. Pressure-induced amorphization and polyamorphism: Inorganic and biochemical system. *Prog. Mater. Sci.* **2014**, *61*, 216.

(18) Somayazulu, M.; Dera, P.; Goncharov, A. F.; Gramsch, S. A.; Liermann, P.; Yang, W.; Liu, Z.; Mao, H. K.; Hemley, R. J. Pressure-induced bonding and compound formation in xenon-hydrogen solids. *Nat. Chem.* **2010**, *2*, 50.

(19) Sun, J.; Klug, D. D.; Pickard, C. J.; Needs, R. J. Controlling the Bonding and Band Gaps of Solid Carbon Monoxide with Pressure. *Phys. Rev. Lett.* **2011**, *106*, 10.1103/PhysRevLett.106.145502.

(20) Eremets, M. I.; Troyan, I. A. Conductive dense hydrogen. *Nat. Mater.* **2011**, *10*, 927.

(21) Dubrovinsky, L.; Dubrovinskaia, N. Comprehensive Inorganic Chemistry II; Elsevier, 2013; Vol. *2*, p 223.

(22) Hemley, R. J. Effects Of High Pressure On Molecules. *Annu. Rev. Phys. Chem.* **2000**, *51*, 763.

(23) Zhang, W. W.; Oganov, A. R.; Goncharov, A. F.; Zhu, Q.; Boulfelfel, S. E.; Lyakhov, A. O.; Stavrou, E.; Somayazulu, M.; Prakapenka, V. B.; Konopkova, Z. Unexpected Stable Stoichiometries of Sodium Chlorides. *Science* **2013**, *342*, 1502.

(24) Recio, J. M.; Menéndez, J. M.; Otero-de-la-Roza, A. *An Introduction to High-Pressure Science and Technology*; CRC Press: Boca Raton, 2015.

(25) Arof, A. K.; Radhakrishna, S. Electrical properties of Silver Vanadate electrochemical-cells. *J. Alloys Compd.* **1993**, *200*, 129.

(26) Chen, L. C.; Pan, G. T.; Yang, T. C. K.; Chung, T. W.; Huang, C. M. In situ DRIFT and kinetic studies of photocatalytic degradation on benzene vapor with visible-light-driven silver vanadates. *J. Hazard. Mater.* **2010**, *178*, 644.

(27) Chen, Z. J.; Gao, S. K.; Li, R. H.; Wei, M.; Wei, K.; Zhou, H. S. Lithium insertion in ultra-thin nanobelts of Ag2V4O11/Ag. *Electrochim. Acta* **2008**, *53*, 8134.

(28) Ju, P.; Fan, H.; Zhang, B. L.; Shang, K.; Liu, T.; Ai, S. Y.; Zhang, D. Enhanced photocatalytic activity of beta-AgVO3 nanowires loaded with Ag nanoparticles under visible light irradiation. *Sep. Purif. Technol.* **2013**, *109*, 107.

(29) Kong, X. G.; Guo, Z. L.; Zeng, C. B.; Huang, J. F.; Cao, L. Y.; Li, L.; Yin, L. X.; Wen, P. H.; Feng, Q.; Xu, Z. W. Soft chemical in situ synthesis, formation mechanism and electrochemical performances of 1D bead-like AgVO3 nanoarchitectures. *J. Mater. Chem. A* **2015**, *3*, 18127.

(30) Liang, S. Q.; Zhou, J.; Pan, A. Q.; Li, Y. J.; Chen, T.; Tian, Z. M.; Ding, H. B. Facile synthesis of beta-AgVO3 nanorods as cathode for primary lithium batteries. *Mater. Lett.* **2012**, *74*, 176.

(31) Mai, L. Q.; Xu, L.; Gao, Q. A.; Han, C. H.; Hu, B.; Pi, Y. Q. Single beta-AgVO3 Nanowire H2S Sensor. *Nano Lett.* **2010**, *10*, 2604.

(32) Pal, S.; Tak, Y. K.; Song, J. M. Does the antibacterial activity of silver nanoparticles depend on the shape of the nanoparticle? A study of the gram-negative bacterium Escherichia coli. *Appl. Environ. Microbiol.* **2007**, *73*, 1712.

(33) Ren, J.; Wang, W. Z.; Shang, M.; Sun, S. M.; Zhang, L.; Chang, J. A. Photocatalytic activity of silver vanadate with one-dimensional structure under fluorescent light. *J. Hazard. Mater.* **2010**, *183*, 950.

(34) Sharma, S.; Panthofer, M.; Jansen, M.; Ramanan, A. Ion exchange synthesis of silver vanadates from organically templated layered vanadates. *Mater. Chem. Phys.* **2005**, *91*, 257.

(35) Shi, H. F.; Li, Z. S.; Kou, J. H.; Ye, J. H.; Zou, Z. G. Facile Synthesis of Single-Crystalline Ag2V4O11 Nanotube Material as a Novel Visible-Light-Sensitive Photocatalyst. *J. Phys. Chem. C* **2011**, *115*, 145.

(36) Sivakumar, V.; Suresh, R.; Giribabu, K.; Narayanan, V. AgVO3 nanorods: Synthesis, characterization and visible light photocatalytic activity. *Solid State Sci.* **2015**, *39*, 34.

DOI: 10.1021/acs.jpcc.7b09865
J. Phys. Chem. C 2017, 121, 27624−27642

(37) Xu, H.; Li, H. M.; Xu, L.; Wu, C. D.; Sun, G. S.; Xu, Y. G.; Chu, J. Y. Enhanced Photocatalytic Activity of Ag3VO4 Loaded with Rare-Earth Elements under Visible-Light Irradiation. *Ind. Eng. Chem. Res.* **2009**, *48*, 10771.
(38) Zeng, H.; Wang, Q.; Rao, Y. Y. Ultrafine beta-AgVO3 nanoribbons derived from alpha-AgVO3 nanorods by water evaporation method and its application for lithium ion batteries. *RSC Adv.* **2015**, *5*, 3011.
(39) Zhao, W.; Guo, Y.; Faiz, Y.; Yuan, W. T.; Sun, C.; Wang, S. M.; Deng, Y. H.; Zhuang, Y.; Li, Y.; Wang, X. M.; He, H.; Yang, S. G. Facile in-suit synthesis of Ag/AgVO3 one-dimensional hybrid nanoribbons with enhanced performance of plasmonic visible-light photocatalysis. *Appl. Catal., B* **2015**, *163*, 288.
(40) Zhao, W.; Guo, Y.; Wang, S. M.; He, H.; Sun, C.; Yang, S. G. A novel ternary plasmonic photocatalyst: ultrathin g-C3N4 nanosheet hybrided by Ag/AgVO3 nanoribbons with enhanced visible-light photocatalytic performance. *Appl. Catal., B* **2015**, *165*, 335.
(41) Wei, Z.; Feng, L.; Zhi-Ming, J.; Xiao-Bo, J.; Peng-Hui, Y.; Xue-Ren, W.; Cheng, S.; Zhan-Qi, G.; Liang-Sheng, L. Efficient plasmonic photocatalytic activity on silver-nanoparticle-decorated AgVO3 nanoribbons. *J. Mater. Chem. A* **2014**, *2*, 13226−13231.
(42) Zhao, W.; Wei, Z. B.; He, H.; Xu, J.; Li, J. H.; Yang, S. G.; Sun, C. Supporting 1-D AgVO3 nanoribbons on single layer 2-D graphitic carbon nitride ultrathin nanosheets and their excellent photocatalytic activities. *Appl. Catal., A* **2015**, *501*, 74.
(43) Fleury, P.; Kohlmull, R. Sur le systeme AG20-V205. *C. R. Hebd. Seances Acad. Sci.* **1966**, *262*, 475.
(44) Cheng, F. Y.; Chen, J. Transition metal vanadium oxides and vanadate materials for lithium batteries. *J. Mater. Chem.* **2011**, *21*, 9841.
(45) Rozier, P.; Galy, J. Ag1.2V3O8 crystal structure: Relationship with Ag2V4O11-y interpretation of physical properties. *J. Solid State Chem.* **1997**, *134*, 294.
(46) Rozier, P.; Savariault, J. M.; Galy, J. beta AgVO3 crystal structure and relationships with Ag2V4O11 and delta AgxV2O5. *J. Solid State Chem.* **1996**, *122*, 303.
(47) Kittaka, S.; Matsuno, K.; Akashi, H. Crystal structure of alpha-AgVO3 and phase relation of AgVO3. *J. Solid State Chem.* **1999**, *142*, 360.
(48) Kittaka, S.; Yata, Y.; Matsuno, K.; Nishido, H. Interaction of Ag ions with a vanadium pentoxide hydrate - Formation of silver vanadate at low temperature. *J. Mater. Sci.* **2000**, *35*, 2185.
(49) Kittaka, S.; Nishida, S.; Iwashita, T.; Ohtani, T. Reactivity and structural properties of a mechanochemically treated Ag2O-V2O5 system in relation to AgVO3 polymorphs. *J. Solid State Chem.* **2002**, *164*, 144.
(50) Mahmood, A.; Ramay, S. M.; Al-Zaghayer, Y. S.; Atiq, S.; Ahmad, I.; Shar, M. A.; Khan, S. D. Study the structure and performance of thermal/plasma modified Au nanoparticle-doped TiO2 photocatalyst. *Mod. Phys. Lett. B* **2014**, *28*, 1450077.
(51) de Oliveira, R. C.; Assis, M.; Teixeira, M. M.; da Silva, M. D. P.; Li, M. S.; Andres, J.; Gracia, L.; Longo, E. An Experimentally and Computational Study of b-AgVO3: Optical Properties and the Formation of Ag Nanoparticles. *J. Phys. Chem. C* **2016**, *120*, 12254.
(52) de Oliveira, R. C.; de Foggi, C. C.; Teixeira, M. M.; da Silva, M. D. P.; Assis, M.; Francisco, E. M.; Pimentel, B.; Pereira, P. F. D.; Vergani, C. E.; Machado, A. L.; Andres, J.; Gracia, L.; Longo, E. Mechanism of Antibacterial Activity via Morphology Change of alpha-AgVO3: Theoretical and Experimental Insights. *ACS Appl. Mater. Interfaces* **2017**, *9*, 11472.
(53) Beltran, A.; Gracia, L.; Longo, E.; Andres. First-Principles Study of Pressure-Induced Phase Transitions and Electronic Properties of Ag2MoO4. *J. Phys. Chem. C* **2014**, *118*, 3724.
(54) Mehl, M. J.; Finkenstadt, D.; Dane, C.; Hart, G. L. W.; Curtarolo, S. Finding the stable structures of N1-xWx with an ab initio high-throughput approach. *Phys. Rev. B: Condens. Matter Mater. Phys.* **2015**, *91*, 10.1103/PhysRevB.91.184110.
(55) Becke, A. D. Density-Functional Thermochemistry. The Role of Exact Exchange. *J. Chem. Phys.* **1993**, *98*, 5648.
(56) Lee, C. T.; Yang, W. T.; Parr, R. G. Development of the Colle-Salvetti Correlation-Energy Formula into a Functional of the Electron-Density. *Phys. Rev. B: Condens. Matter Mater. Phys.* **1988**, *37*, 785.
(57) Heyd, J.; Scuseria, G. E.; Ernzerhof, M. Hybrid functionals based on a screened Coulomb potential. *J. Chem. Phys.* **2003**, *118*, 8207.
(58) Krukau, A. V.; Vydrov, O. A.; Izmaylov, A. F.; Scuseria, G. E. Influence of the exchange screening parameter on the performance of screened hybrid functionals. *J. Chem. Phys.* **2006**, *125*, 22410610.1063/1.2404663.
(59) Perdew, J. P.; Wang, Y. Accurate and simple analytic representation of the electron-gas correlation-energy. *Phys. Rev. B: Condens. Matter Mater. Phys.* **1992**, *45*, 13244.
(60) Dovesi, R.; Saunders, V. R.; Roetti, C.; Orlando, R.; Zicovich-Wilson, C. M.; Pascale, F.; Civalleri, B.; Doll, K.; Harrison, N. M.; Bush, I. J.; D'Arco, P.; Llunell, M.; Causà, M.; Noël, Y. CRYSTAL14 User's Manual; University of Torino: Torino, 2014.
(61) Santra, B.; Klimes, J.; Alfe, D.; Tkatchenko, A.; Slater, B.; Michaelides, A.; Car, R.; Scheffler, M. Hydrogen Bonds and van der Waals Forces in Ice at Ambient and High Pressures. *Phys. Rev. Lett.* **2011**, *107*, 10.1103/PhysRevLett.107.185701.
(62) Grimme, S. Semiempirical GGA-type density functional constructed with a long-range dispersion correction. *J. Comput. Chem.* **2006**, *27*, 1787.
(63) Bucko, T.; Hafner, J.; Lebegue, S.; Angyan, J. G. Improved Description of the Structure of Molecular and Layered Crystals: Ab Initio DFT Calculations with van der Waals Corrections. *J. Phys. Chem. A* **2010**, *114*, 11814.
(64) http://www.crystal.unito.it/Basis_Sets/Ptable.html.
(65) Erba, A.; Mahmoud, A.; Belmonte, D.; Dovesi, R. High pressure elastic properties of minerals from ab initio simulations: The case of pyrope, grossular and andradite silicate garnets. *J. Chem. Phys.* **2014**, *140*, 12470310.1063/1.4869144.
(66) Birch, F. Finite Elastic Strain Of Cubic Crystals. *Phys. Rev.* **1947**, *71*, 809.
(67) Birch, F. Finite Strain Isotherm And Velocities For Single-Crystal And Polycristalline NaCl At High-Pressures And 300-Degree-K. *J. Geophys. Res.* **1978**, *83*, 1257.
(68) Bocharov, D.; Gryaznov, D.; Zhukovskii, Y. F.; Kotomin, E. A. Ab initio Modeling of Oxygen Impurity Atom Incorporation into Uranium Mononitride Surface and Sub-Surface Vacancies. *J. Nucl. Mater.* **2011**, *416*, 200.
(69) Dorado, B.; Freyss, M.; Martin, G. GGA plus U Study of the Incorporation of Iodine in Uranium Dioxide. *Eur. Phys. J. B* **2009**, *69*, 203.
(70) Lee, Y. L.; Kleis, J.; Rossmeisl, J.; Morgan, D. Ab initio Energetics of LaBO3(001)(B = Mn, Fe, Co, and Ni) for Solid Oxide Fuel Cell Cathodes. *Phys. Rev. B: Condens. Matter Mater. Phys.* **2009**, *80*, 224101.
(71) Martinez, J. I.; Hansen, H. A.; Rossmeisl, J.; Norskov, J. K. Formation Energies of Rutile Metal Dioxides Using Density Functional Theory. *Phys. Rev. B: Condens. Matter Mater. Phys.* **2009**, *79*, 045120.
(72) Takeuchi, K. J.; Marschilok, A. C.; Davis, S. M.; Leising, R. A.; Takeuchi, E. S. Silver vanadium oxides and related battery applications. *Coord. Chem. Rev.* **2001**, *219*, 283−310.
(73) Curnan, M. T.; Kitchin, J. R. Investigating the Energetic Ordering of Stable and Metastable TiO2 Polymorphs Using DFT plus U and Hybrid Functionals. *J. Phys. Chem. C* **2015**, *119*, 21060.
(74) Gerosa, M.; Bottani, C. E.; Caramella, L.; Onida, G.; Di Valentin, C.; Pacchioni, G. Electronic structure and phase stability of oxide semiconductors: Performance of dielectric-dependent hybrid functional DFT, benchmarked against GW band structure calculations and experiments. *Phys. Rev. B: Condens. Matter Mater. Phys.* **2015**, *91*, 10.1103/PhysRevB.91.155201.
(75) Labat, F.; Baranek, P.; Domain, C.; Minot, C.; Adamo, C. Density functional theory analysis of the structural and electronic properties of TiO2 rutile and anatase polytypes: Performances of different exchange-correlation functionals. *J. Chem. Phys.* **2007**, *126*, 15470310.1063/1.2717168.

DOI: 10.1021/acs.jpcc.7b09865
J. Phys. Chem. C 2017, 121, 27624−27642

(76) Landmann, M.; Rauls, E.; Schmidt, W. G. The electronic structure and optical response of rutile, anatase and brookite TiO2. *J. Phys.: Condens. Matter* **2012**, *24*, 19550310.1088/0953-8984/24/19/195503.
(77) Muscat, J.; Swamy, V.; Harrison, N. M. First-principles calculations of the phase stability of TiO2. *Phys. Rev. B: Condens. Matter Mater. Phys.* **2002**, *65*, 10.1103/PhysRevB.65.224112.
(78) Ochoa-Calle, A. J.; Zicovich-Wilson, C. M.; Hernandez-Lamoneda, R.; Ramirez-Solis, A. Understanding the epsilon and zeta High-Pressure Solid Phases of Oxygen. Systematic Periodic Density Functional Theory Studies Using Localized Atomic Basis. *J. Chem. Theory Comput.* **2015**, *11*, 1195.
(79) Ricca, C.; Ringuede, A.; Cassir, M.; Adamo, C.; Labat, F. A Comprehensive DFT Investigation of Bulk and Low-Index Surfaces of ZrO2 Polymorphs. *J. Comput. Chem.* **2015**, *36*, 9.
(80) Yu, H. Y. S.; Li, S. H. L.; Truhlar, D. G. Perspective: Kohn-Sham density functional theory descending a staircase. *J. Chem. Phys.* **2016**, *145*, 13090110.1063/1.4963168.
(81) Schindlmayr, A. In *Many-Electron Approaches in Physics, Chemistry and Mathematics*; Site, V. B. a. L. D., Ed.; Springer International: Cham, Switzerland, 2014; Vol. *29*, p 343.
(82) Bilbao Crystallographic Server: IR Raman Hyper Raman modes. http://www.cryst.ehu.es/cgi-bin/cryst/programs//nph-sam.
(83) McNulty, D.; Ramasse, Q.; O'Dwyer, C. The structural conversion from alpha-AgVO3 to beta-AgVO3: Ag nanoparticle decorated nanowires with application as cathode materials for Li-ion batteries. *Nanoscale* **2016**, *8*, 16266.
(84) Badger, R. A Relation Between Internuclear Distances and Bond Force Constants. *J. Chem. Phys.* **1934**, *2* (128), 1749433.
(85) Konta, R.; Kato, H.; Kobayashi, H.; Kudo, A. Photophysical properties and photocatalytic activities under visible light irradiation of silver vanadates. *Phys. Chem. Chem. Phys.* **2003**, *5*, 3061.
(86) Schweitzer, C.; Reimann, K.; Steube, M. Two-photon spectroscopy of SnO 2 under hydrostatic pressure. *Solid State Commun.* **1999**, *110*, 697.
(87) Pisani, C.; Dovesi, R.; Roetti, C. *Hartree-Fock Ab Initio Treatment of Crystalline Systems*; Springer: Berlin, 1988; Vol. *48*.

DOI: 10.1021/acs.jpcc.7b09865
J. Phys. Chem. C 2017, 121, 27624−27642